Aluminum Alloys: Metallographic Techniques and Microstructures
Revised by Richard H. Stevens, Aluminum Company of America

<Previous section in this article

Atlas of Microstructures for Aluminum Alloys

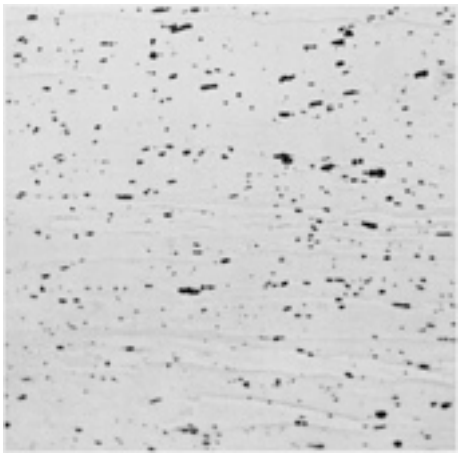

Fig. 1 Alloy 1100-H18 sheet, cold rolled. Note metal flow around insoluble particles of $FeAl_3$ (black). Particles are remnants of scriptlike constituents in the ingot that have been fragmented by working. See also Fig. 2. 0.5% HF. 500×

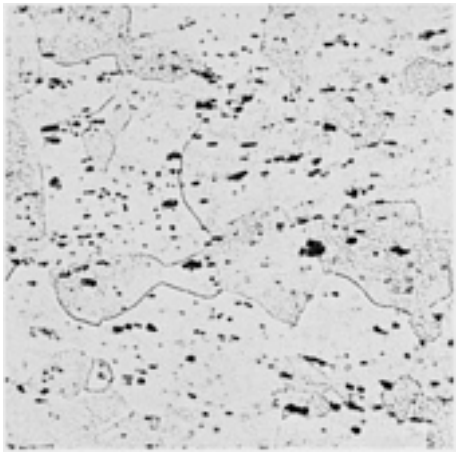

Fig. 2 Alloy 1100-O sheet, cold rolled and annealed. Recrystallized, equiaxed grains and insoluble particles of $FeAl_3$ (black). Size and distribution of Fe-Al_3 in the worked structure were unaffected by annealing (see also Fig. 1). 0.5% HF. 500×

Fig. 3 Alloy 3003-F tube, extruded through a two-port bridge die. The bands of fine precipitate

show pattern of metal flow and the areas where the metal entering through the two ports was welded together in the die. Caustic fluoride. 5×

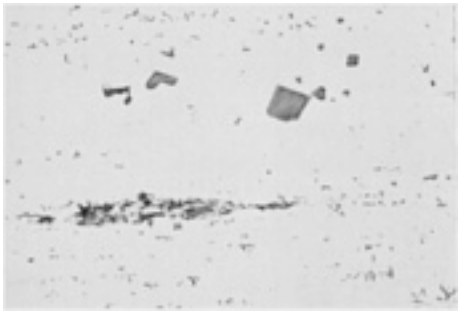

Fig. 4 Alloy 3003-F sheet, hot rolled. Longitudinal section shows stringer of oxide from an inclusion in the cast ingot and particles of phases that contain manganese, both primary (large, angular) and eutectic (small). As-polished. 500×

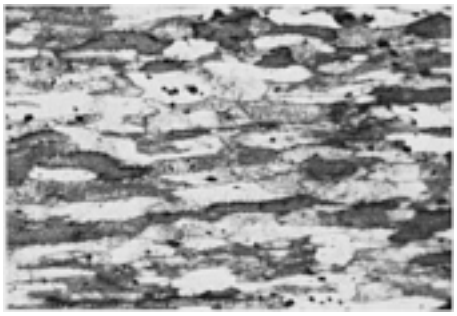

Fig. 5 Alloy 3003-O sheet, annealed. Longitudinal section shows recrystallized grains. Grain elongation indicates rolling direction, but not the crystallographic orientation within each grain. Polarized light. Barker's reagent. 100×

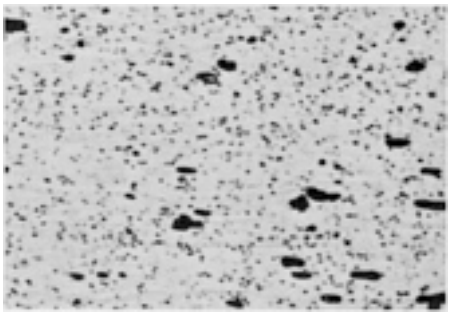

Fig. 6 Same alloy and condition as for Fig. 5, but shown at a higher magnification. Dispersion of insoluble particles of $(Fe,Mn)Al_6$ (large) and aluminum-manganese-silicon (both large and small) was not changed by annealing. 0.5% HF. 750×

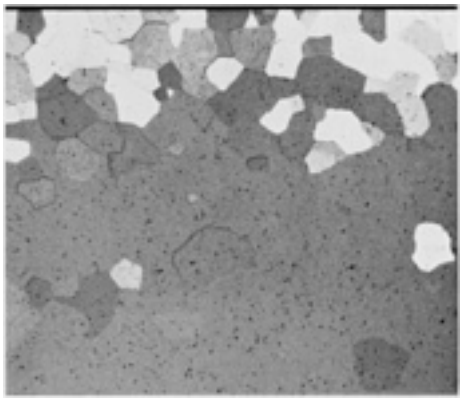

Fig. 7 Alloy 5457-F extrusion. A transverse section, photographed with polarized light. Surface

grains (top) show random reflection, indicating random crystallographic orientation; interior grains show uniform reflection, indicating a high degree of preferred orientation. Barker's reagent. 100×

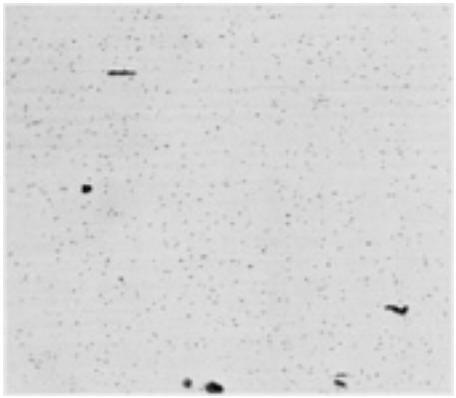

Fig. 8 Alloy 5457-F plate 6.4-mm (0.25-in.) thick, hot rolled. Fine particles of Mg_2Si precipitated during the rolling. If carried through to final sheet, this amount of precipitate would cause an objectionable milky appearance in a subsequently applied anodic coating. 0.5% HF. 500×

[graphic]

Fig. 9 Alloy 5457-O plate 10-mm (0.4-in.) thick, longitudinal section. Annealed at 345 °C (650 °F). Polarized light. The grains are equiaxed. See also Fig. 10, 11, and 12. Barker's reagent. 100×

[graphic]

Fig. 10

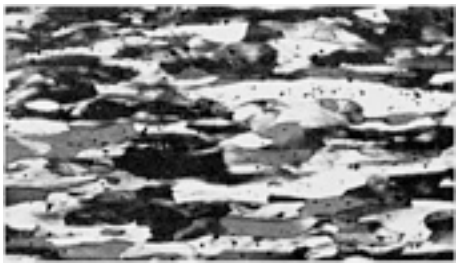

Fig. 11

Fig. 12

Effect of cold rolling on alloy 5457-O plate, originally 10-mm (0.4-in.) thick, annealed at 345 °C (650 °F). Polarized light. See Fig. 9 for annealed structure. Fig. 10: 10% reduction. Fig. 11: 40% reduction. Fig. 12: 80% reduction. Barker's reagent. 100×

[graphic]

Fig. 13 Alloy 5657-F sheet, cold rolled (85% reduction). Longitudinal section. Polarized light. Grains are greatly elongated and contribute to high strength, but ductility is lower than for specimen in Fig. 15. Barker's reagent. 100×

[graphic]

Fig. 14 Same alloy and reduction as Fig. 13, stress relieved at 300 °C (575 °F) for 1 h. Polarized light. Structure shows onset of recrystallization, which improves formability. Barker's reagent. 100×

[graphic]

Fig. 15 Same alloy and reduction as Fig. 13, annealed at 315 °C (600 °F) for 1 h. Polarized light. Recrystallized grains and bands of unrecrystallized grains. Barker's reagent. 100×

[graphic]

Fig. 16 Alloy 5657 ingot. Dendritic segregation (coring) of titanium. Black spots are etch pits. Anodized coating from Barker's reagent was stripped with 10% H_3PO_4 at 80 °C (180 °F). 200×

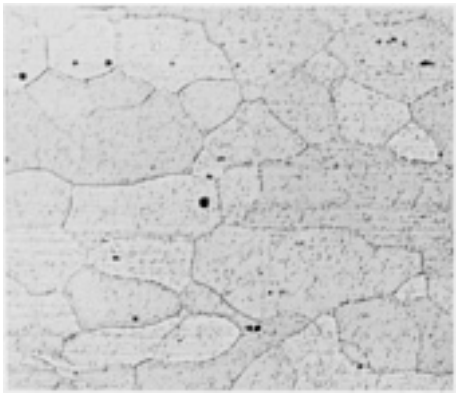

Fig. 17 Alloy 5657 sheet. Banding from dendritic segregation (coring) of titanium in the ingot (see Fig. 16). Anodized coating from Barker's reagent was stripped with 10% H_3PO_4 at 80 °C (180 °F). 200×

[graphic]

Fig. 18 Alloy 5454, hot-rolled slab, longitudinal section. Oxide stringer from an inclusion in the cast ingot. The structure also shows some particles of $(Fe,Mn)Al_6$ (light gray). As-polished. 500×

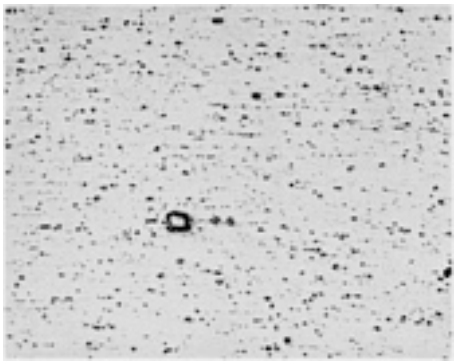

Fig. 19 Alloy 5083-H112 plate, cold rolled. Longitudinal section shows particles of primary $MnAl_6$ (gray, outlined). Small, dark areas may be particles of insoluble phases, such as phases that contain magnesium (for example, Mg_2Si) or that contain manganese. Keller's reagent. 50×

[graphic]

Fig. 20 Alloy 5083 plate, cold rolled. The coarse, gray areas are particles of insoluble $(Fe,Mn)_3SiAl_{12}$; adjacent black areas are voids caused by breakup of the brittle $(Fe,Mn)_3SiAl_{12}$ particles during cold rolling. Separate black areas may be insoluble particles of Mg_2Si. As-polished. 500×

[graphic]

Fig. 21 Alloy 5086-H34 plate, 13-mm (0.5-in.) thick, cold rolled and stabilized at 120 to 175 °C (250 to 350 °F) to prevent age softening. Undesirable continuous network of Mg_2Al_3 particles precipitated at grain boundaries; large particles are insoluble phases. See also Fig. 23. 25% HNO_3. 250×

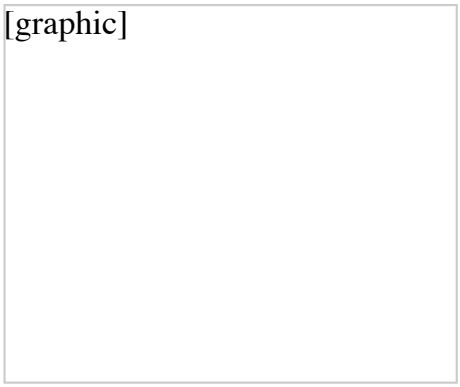

Fig. 22 Alloy 5456 plate, hot rolled. Longitudinal section. Polarized light. Partial recrystallization occurred immediately after hot rolling from residual heat. This type of recrystallization is frequently referred to as "dynamic recrystallization." Barker's reagent. 100×

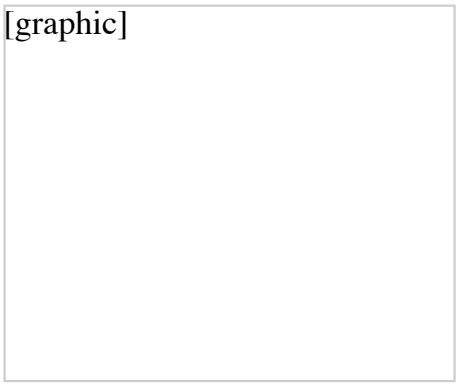

Fig. 23 Alloy 5456 plate, 6.4 mm (0.25 in.) thick, cold rolled and stress relieved below the solvus at 245 °C (475 °F). Particles are $(Fe,Mn)Al_6$ (gray), Mg_2Si (black), and Mg_2Al_3 (fine precipitate). In contrast to Fig. 21, there is no continuous network of precipitate at grain boundaries. 25% HNO_3. 500×

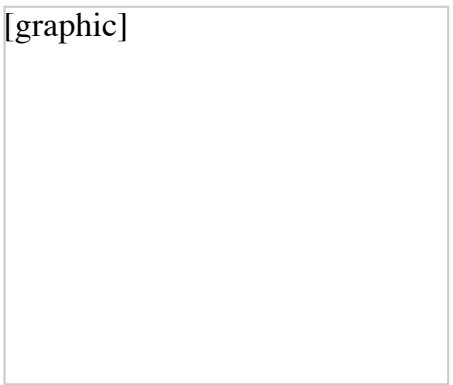

Fig. 24 Alloy 5456-O plate, 13 mm (0.5 in.) thick, hot rolled, and annealed above the solvus. Rapid cooling resulted in retention of Mg_2Al_3 in solid solution. The light, outlined particles are insoluble $(Fe,Mn)Al_6$; the dark particles are insoluble Mg_2Si. 25% HNO_3. 500×

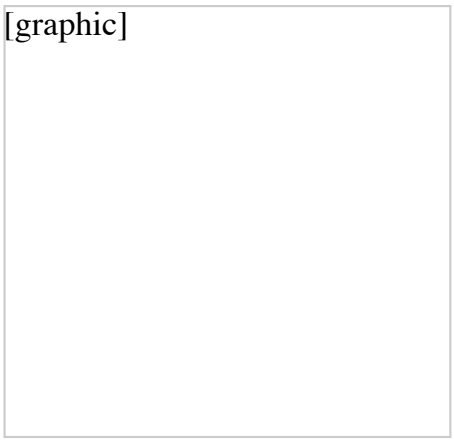

Fig. 25 Alloy 2014-T4 closed die forging, solution heat treated at 500 °C (935 °F) for 2 h and quenched in water at 60 to 70 °C (140 to 160 °F). Longitudinal section. Structure contains particles of $CuAl_2$ (white, outlined) and insoluble $(Fe,Mn)_3SiAl_{12}$ (dark). Keller's reagent. 100×

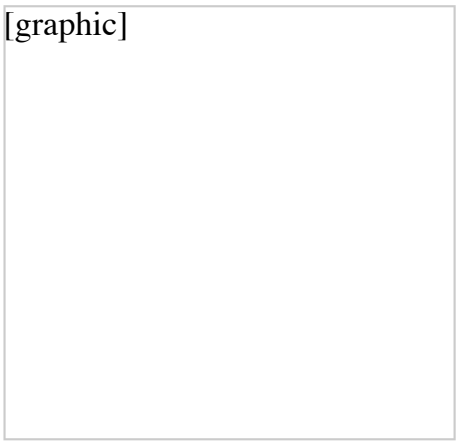

Fig. 26 Alloy 2014-T6 closed-die forging, solution heat treated, then aged at 170 °C (340 °F) for 10 h. Longitudinal section. Fragmented grain structure; constituents are same as for Fig. 25, but very fine particles of $CuAl_2$ have precipitated in the matrix. Keller's reagent. 100×

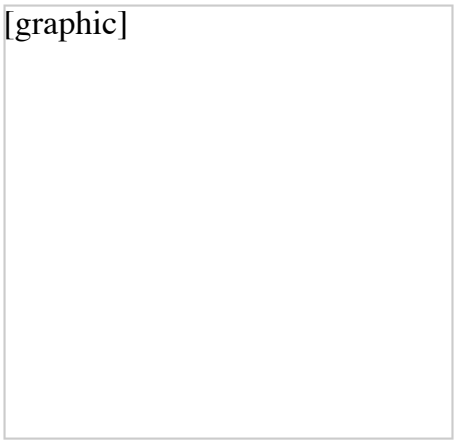

Fig. 27 Alloy 2014-T6 closed-die forging, overaged. Solution heat treatment was sufficient, but specimen was overaged. Fragmented grain structure; constituents are same as for Fig. 26, but more $CuAl_2$ has precipitated. Note lack of grain contrast. Keller's reagent. 100×

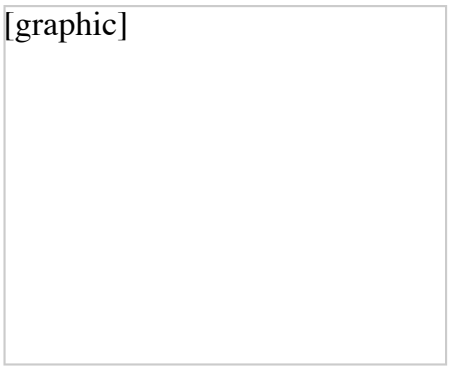

Fig. 28 Alloy 2014-T4 closed-die forging that received insufficient solution heat treatment. Longitudinal section. Constituents are the same as for Fig. 25, but more $CuAl_2$ is visible, because less is in solution. Keller's reagent. 250×

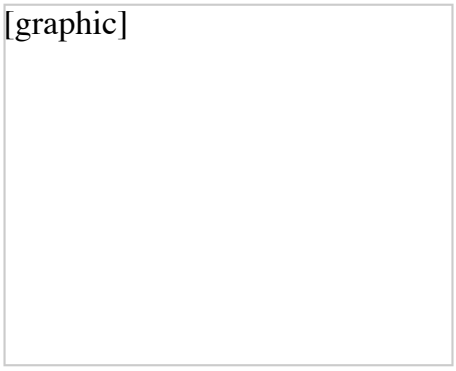

Fig. 29 Alloy 2014-T6 closed-die forging, showing rosettes formed by eutectic melting. Solidus temperature (510 °C, or 950 °F) was exceeded during solution heat treating. Other constituents are the same as in Fig. 26. Keller's reagent. 500×

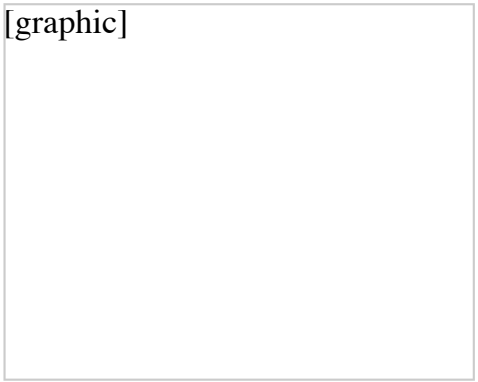

Fig. 30 Alloy 2014-T6 closed-die forging. Hydrogen porosity (black), and particles of $(Fe,Mn)_3SiAl_{12}$ (gray) and $CuAl_2$ (gray, speckled) are visible. As-polished. 250×

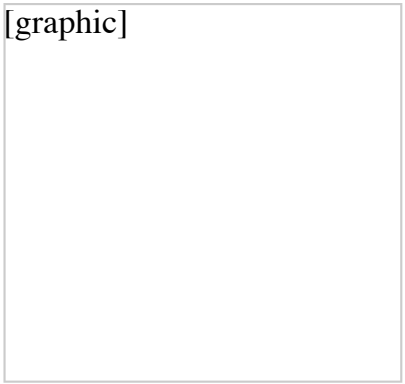

Fig. 31 Alloy 2014-T61 closed-die forging. Blister on surface is associated with hydrogen porosity. As-polished. 50×

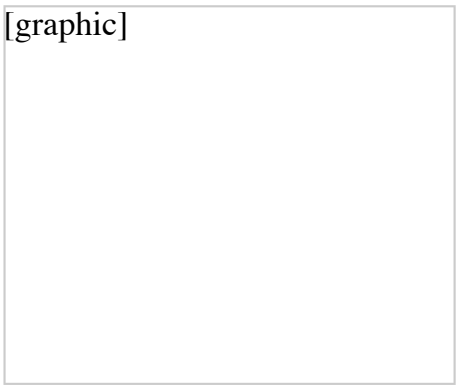

Fig. 32 Alloy 2024-T3 sheet, solution heat treated at 495 °C (920 °F) and quenched in cold water. Longitudinal section. Dark particles are $CuMgAl_2$, Cu_2MnAl_{20}, and Cu_2FeAl_7. Keller's reagent. See also Fig. 33. 500×

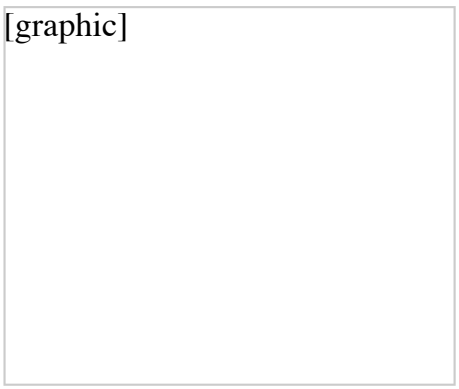

Fig. 33 Same alloy and solution heat treatment as Fig. 32, but quenched in boiling water. The lower quenching rate resulted in precipitation of $CuMgAl_2$ at grain boundaries. Keller's reagent. 500×

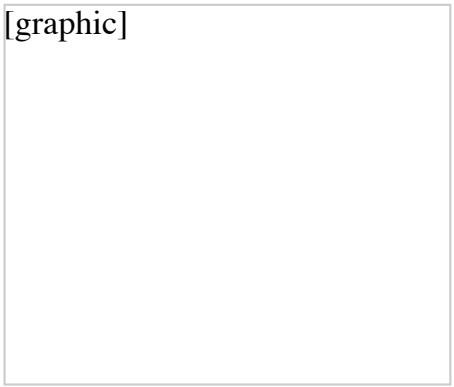

Fig. 34 Same alloy and solution heat treatment as Fig. 32, but cooled in an air blast. The lower cooling rate resulted in increased precipitation of $CuMgAl_2$ at grain boundaries. Keller's reagent. 500×

[graphic]

Fig. 35 Same alloy and solution heat treatment as Fig. 32, but cooled in still air. The slow cooling resulted in intragranular and grain-boundary precipitation of $CuMgAl_2$. Keller's reagent. 500×

[graphic]

Fig. 36 Alloy 2024-T3 sheet clad with alloy 1230 (5% per side), solution heat treated. Normal amount of copper and magnesium diffusion from base metal into cladding (top). Keller's reagent. 100×

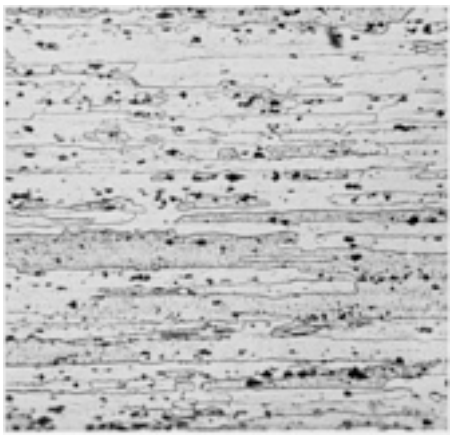

Fig. 37 2024-T6 sheet, 6.4 mm (0.25 in.) thick (reduced from 406-mm, or 16-in. thick ingot), stretched 2%. Longitudinal section. Note absence of strain lines in structure. See also Fig. 38 and 39. Keller's reagent. 100×

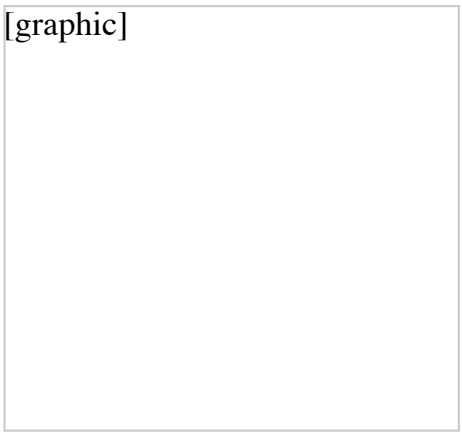
[graphic]

Fig. 38 Same as Fig. 37, but stretched 6%. Longitudinal section. Some faint strain lines have formed. See also Fig. 39. Keller's reagent. 100×

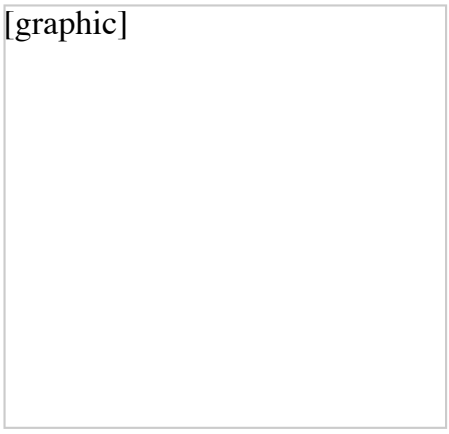
[graphic]

Fig. 39 Same as Fig. 37, but stretched 20%. Longitudinal section. Many strain lines have formed. See also Fig. 38. Keller's reagent. 100×

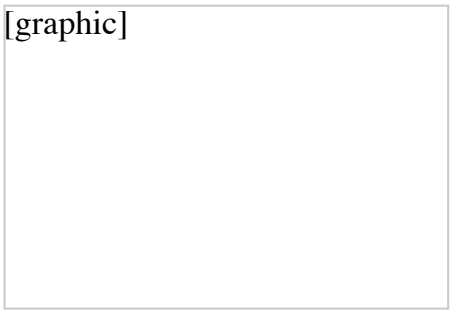
[graphic]

Fig. 40 Alloy 2024-T851 plate, 150 mm (6 in.) thick, cold rolled, solution heat treated, stretched and artificially aged. Section was taken in the rolling plane (long transverse) from an area near the surface showing elongated grains. Keller's reagent. 200×

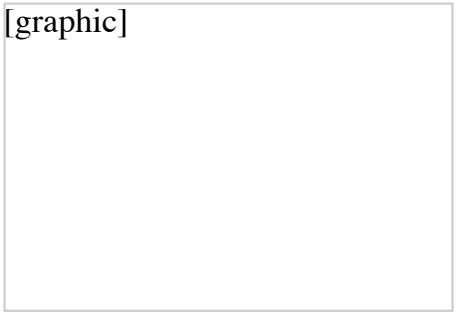
[graphic]

Fig. 41 Same alloy and condition as Fig. 40, but a longitudinal section showing the edge view of an area near the surface of the plate. Grains are flattened and elongated in the direction of rolling. See

also Fig. 42. Keller's reagent. 200×

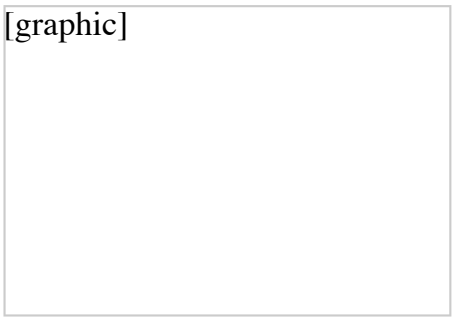

Fig. 42 Same alloy and condition as Fig. 40, but a short transverse section showing the end view of an area near the surface of the plate. Grains are flattened, but are not as elongated as grains in Fig. 41. Keller's reagent. 200×

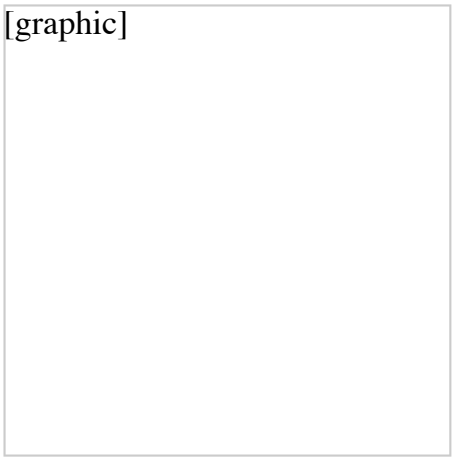

Fig. 43 Same alloy, condition, and orientation as Fig. 40, but specimen was from the center of the plate thickness, which received less cold working than the surface. Keller's reagent. 200×

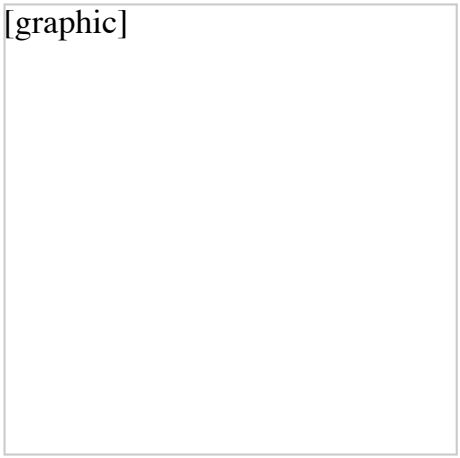

Fig. 44 Same alloy, condition, and orientation as Fig. 41, but specimen was from the center of the plate thickness. There is less flattening and elongation of the grains. Keller's reagent. 200×

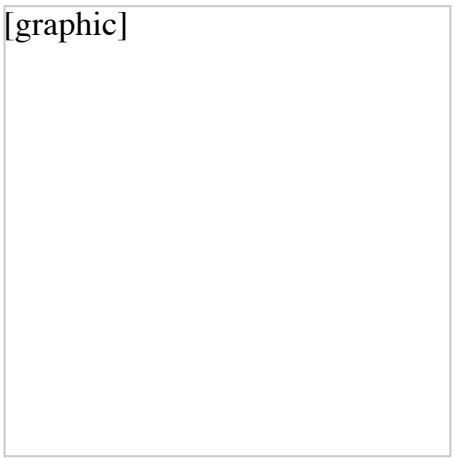
[graphic]

Fig. 45 Same alloy, condition, and orientation as Fig. 42, but specimen was taken from the center of the plate thickness. Less coldworking resulted in less deformation. Keller's reagent. 200×

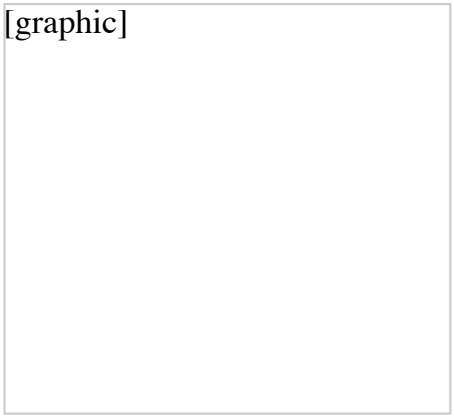
[graphic]

Fig. 46 Alloy 2024-T851 plate, 100 mm (4 in.) thick, hot rolled, solution heat treated, stretched, and artificially aged. Fragmented grain structure; one small recrystallized grain. High rolling temperature limited strain and recrystallization. 10% H_3PO_4. 500×

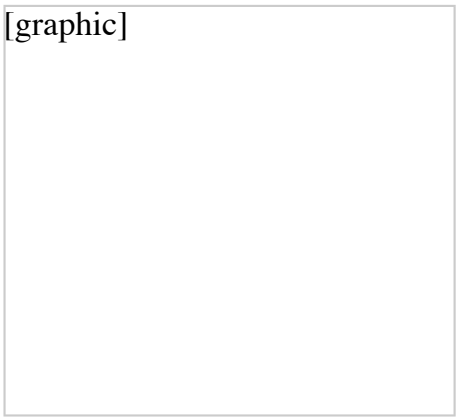
[graphic]

Fig. 47 Alloy 2024-O plate, 13mm ($\frac{1}{2}$ in.) thick, hot rolled and annealed. Longitudinal section. Elongated recrystallized grains and unrecrystallized stringers resulting from polygonization that occurred during the hot water working. $KMnO_4$, Na_2CO_3. 100×

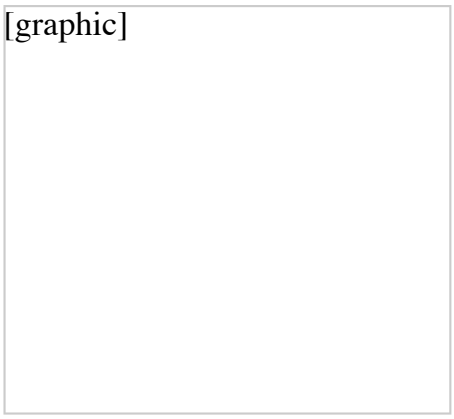

Fig. 48 Alloy 2024-O sheet. Structure consists of light gray particles of insoluble (Cu, Fe,Mn)Al_6, large black particles of undissolved $CuMgAl_2$, and fine particles of $CuMgAl_2$ that precipitated during annealing. 25% HNO_3. 500×

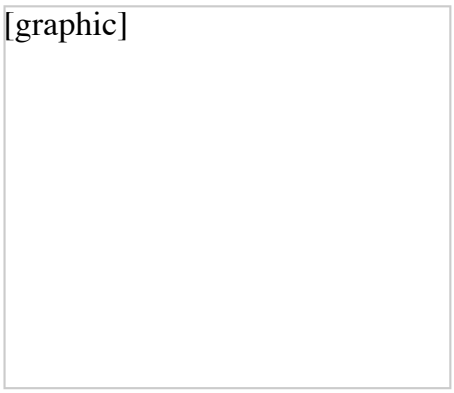

Fig. 49 Alloy 2025-T6 closed-die forging, solution heat treated and artificially aged. Longitudinal section. Complete recrystallization resulted from high residual strain in the forging before solution treatment. See also Fig. 50. Keller's reagent. 100×

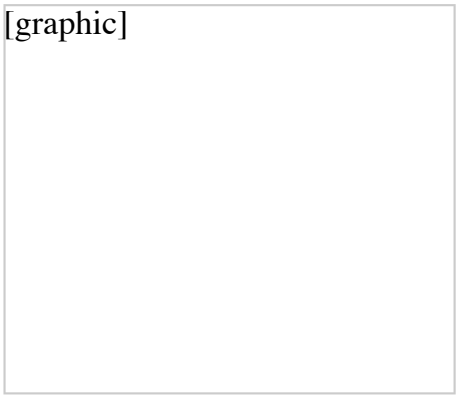

Fig. 50 Same alloy and heat treatment as Fig. 49, but worked structure is only partly recrystallized. Incomplete recrystallization occurred because forging had lower residual strain before solution heat treatment than in Fig. 49. Keller's reagent. 100×

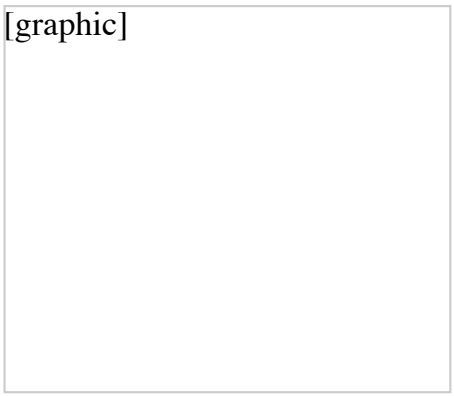

Fig. 51 Alloy 2117-T4 rivet, cold upset, solution heat treated at 500 °C (935 °F) for 35 min, quenched in water at 25 °C (75 °F) max. The small recrystallized grains are in the rivet head, and the large grains are in the shank. Keller's reagent. 60×

Fig. 52 Alloy 2218-T61 closed-die forging, solution heat treated and artificially aged. Fine, recrystallized structure. The dark particles of insoluble $FeNiAl_9$ phase show banding, which resulted from the working during forging. Keller's reagent. 100×

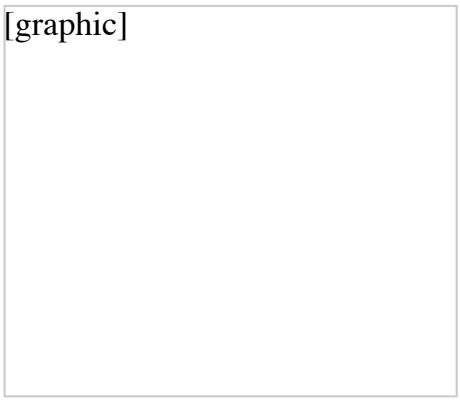

Fig. 53 Alloy 2219-T6 closed-die forging, solution heat treated and artificially aged. Longitudinal section. Worked structure contains some recrystallized grains. See Fig. 54 for a totally unrecrystallized structure. Keller's reagent. 100×

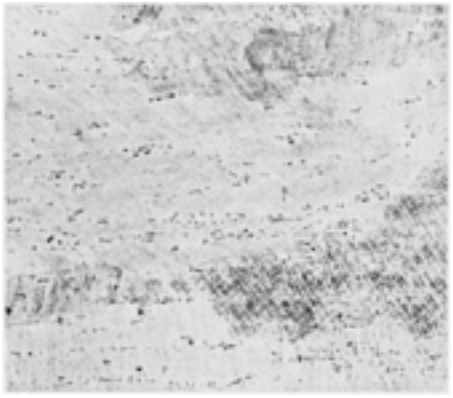

Fig. 54 Same alloy and heat treatment as Fig. 53, but showing no recrystallization of the worked structure. Note the large amount of slip (light parallel lines) that has occurred on two sets of slip planes. Keller's reagent. 100×

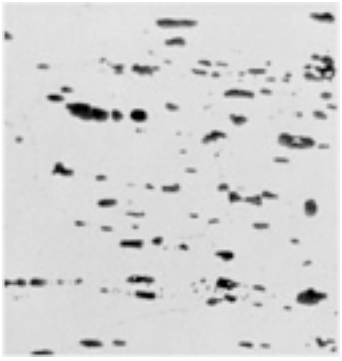

Fig. 55 Alloy 2618-T4 closed-die forging, solution heat treated at 530 °C (985 °F) for 2 h, quenched in boiling water. Small particles of $CuMgAl_2$ precipitated at grain boundaries; larger particles are insoluble $FeNiAl_9$ phase. 0.5% HF. 500×

[graphic]

Fig. 56 Alloy 2618-T4 forging, solution heat treated at 530 °C (985 °F) for 2 h and cooled in still air. Same constituents as Fig. 55, but slower cooling resulted in an increase of $CuMgAl_2$ at grain boundaries and within grains. 0.5% HF. 500×

[graphic]

Fig. 57 Alloy 2618-T61 forging, solution heat treated, quenched in boiling water, aged at 200 °C (390 °F) for 20 h, stabilized at 230 °C (450 °F) for 7 h. Constituents same as Fig. 55; $CuMgAl_2$ has also precipitated in grains. 0.5% HF. 500×

[graphic]

Fig. 58 Alloy 2618-T61 forging, solution heat treated, cooled in still air, aged, and stabilized as described for Fig. 57. Constituents are same as for Fig. 57. Note increase in precipitation and alloy depletion near light grain boundaries. 0.5% HF. 500×

[graphic]

Fig. 59 Alloy 6061-F plate, 38 mm (1.5 in.) thick, as hot rolled (91% reduction). Longitudinal section from center of plate thickness. Particles are Fe_3SiAl_{12} (gray, scriptlike) and Mg_2Si (black). See also Fig. 60 and 61. 0.5% HF. 250×

[graphic]

Fig. 60 Same alloy and condition as Fig. 59, but a longitudinal section from near plate surface. Particles of Fe_3SiAl_{12} and Mg_2Si are more broken up and uniformly distributed than in Fig. 59 (midthickness) See also Fig. 61. 0.5% HF. 250×

[graphic]

Fig. 61 Alloy 6061-F 6.4-mm (0.25-in.) sheet, hot rolled (reduced 98%); midthickness longitudinal

section. Fe_3SiAl_{12} and Mg_2Si particles more broken and dispersed than in Fig. 60. Most Mg_2Si will dissolve during solution treating. 0.5% HF. 250×

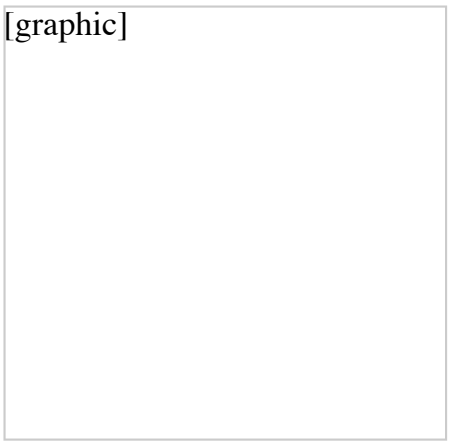
[graphic]

Fig. 62 Alloy 6063-T5 extrusion. Transverse section. Grains at surface of extrusion have recrystallized because of more working and heating. Grains in the interior of the extrusion are unrecrystallized. Tucker's reagent. Actual size

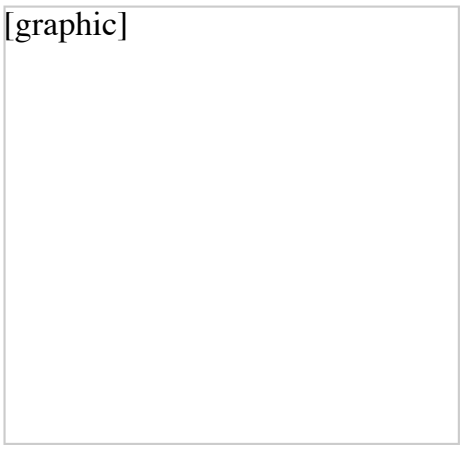
[graphic]

Fig. 63 Alloy 6151-T6 closed-die forging showing large particles of Mg_2Si (rounded) and $(Fe,Mn)_3SiAl_{12}$ (angular or scriptlike), and a fine, banded dispersion of extremely small particles of a chromium intermetallic phase. Keller's reagent. 250×

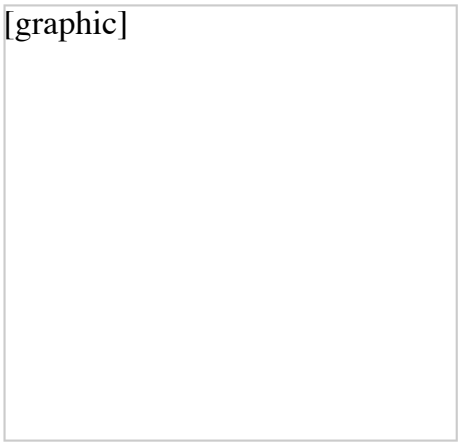
[graphic]

Fig. 64 Alloy 6351-T6 extruded tube, 1.5-mm (0.06-in.) wall. Longitudinal section. Polarized light. Coarse, recrystallized grains at top are near surface; polygonized subgrains are in unrecrystallized interior. Barker's reagent. 100×

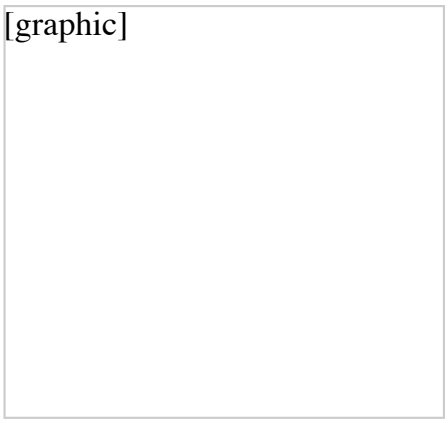
[graphic]

Fig. 65 Alloy 7079-T6 forging, reduced 40%, solution heat treated and artificially aged. Precipitation of Al-Cr-Mn phase (darker areas in structure) occurred during homogenization and is evidence of dendritic coring. NaOH,NaF. 50×

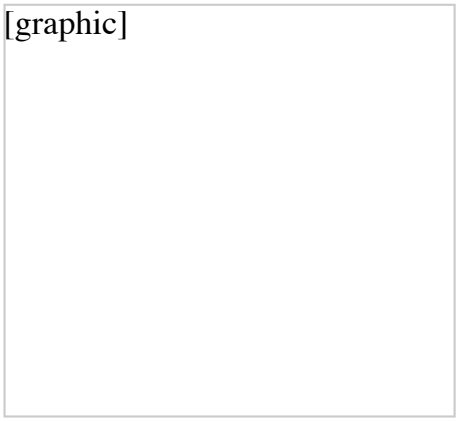
[graphic]

Fig. 66 Alloy 7079-T6 forging, reduced 70%, solution heat treated and artificially aged. Grains are more elongated and thinned than in Fig. 65 because of greater amount of work. Dendritic coring is still evident. NaOH,NaF. 50×

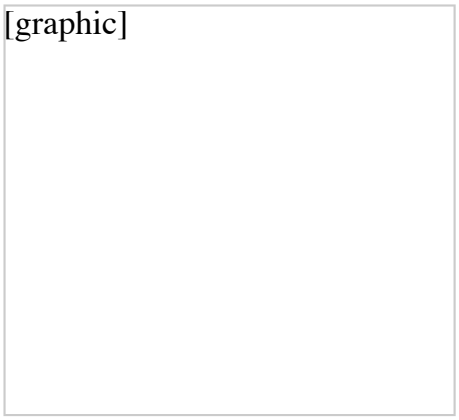
[graphic]

Fig. 67 Alloy 7079-T6 forging, reduced 85%, solution heat treated, and artificially aged. No recrystallization has occurred, because high forging temperature resulted in low residual strain. Note dendritic coring. NaOH,NaF. 50×

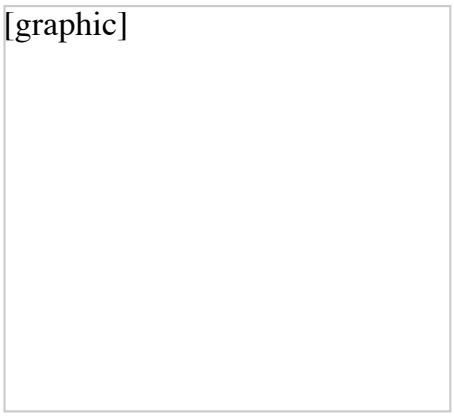

Fig. 68 Alloy 7039 ingot 305 mm (12 in.) thick. Polarized light. Structure shows equiaxed grains with interdendritic areas of Mg_2Si and Fe_3SiAl_{12}. See also Fig. 71. Barker's reagent. 500×

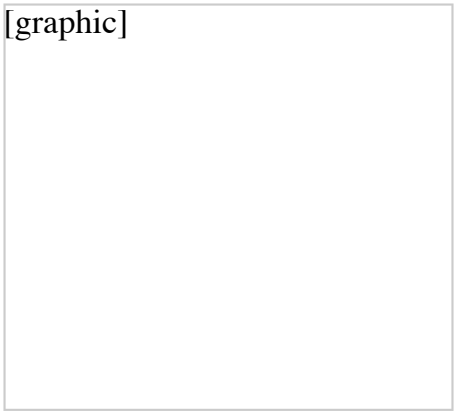

Fig. 69 Alloy 7039-F plate, 150 mm (6 in.) thick, as hot rolled (50% reduction). Polarized light. Grains are elongated and thinned by working. See also Fig. 72. Barker's reagent. 50×

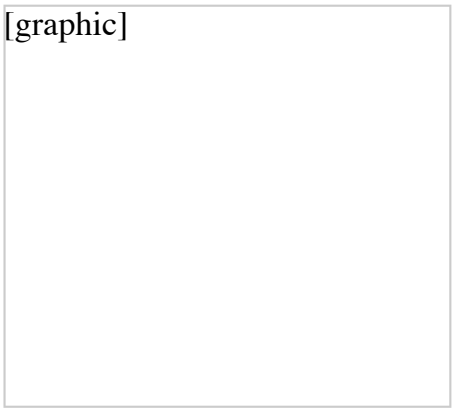

Fig. 70 Alloy 7039-F plate, 50 mm (2 in.) thick, as hot rolled (83% reduction). Polarized light. Grains are greatly elongated and thinned. See also Fig. 73. Barker's reagent. 50×

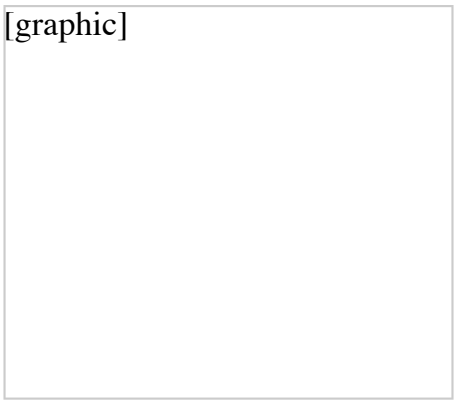
[graphic]

Fig. 71 Alloy 7039 ingot, 305 mm (12 in.) thick. Dendritic cells are more evident than in Fig. 68 because of the higher magnification and the etchant used. Dendritic cells also show precipitate formed during homogenization. 10% H_3PO_4. 100×


[graphic]

Fig. 72 Alloy 7039-F plate, 150 mm (6 in.) thick, as hot rolled (50% reduction). Dendritic cells are elongated and thinned by working. See also Fig. 69. 10% H_3PO_4. 100×

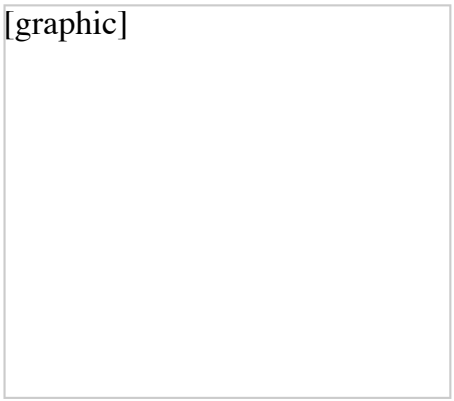
[graphic]

Fig. 73 Alloy 7039-F plate, 50 mm (2 in.) thick, as hot rolled (83% reduction). Dendritic cells are elongated and thinned by working. See also Fig. 70. 10% H_3PO_4. 100×


[graphic]

Fig. 74 Alloy 7075-O sheet, annealed. The fine particles of $MgZn_2$ (dark) were precipitated at lower temperatures during heating to or cooling from the annealing temperature. The insoluble particles of $FeAl_3$ (light gray, outlined) were not affected by the annealing treatment. See also Fig. 75. 25% HNO_3. 500×

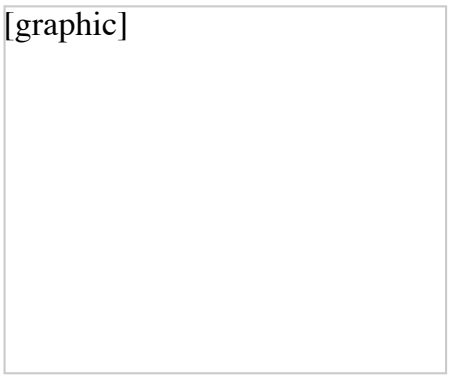

Fig. 75 Alloy 7075-O sheet, annealed, cooled more slowly from annealing temperature than specimen in Fig. 74. Constituents are the same as for Fig. 74. Platelets of $MgZn_2$ precipitated at grain boundaries during slow cooling. 25% HNO_3. 500×

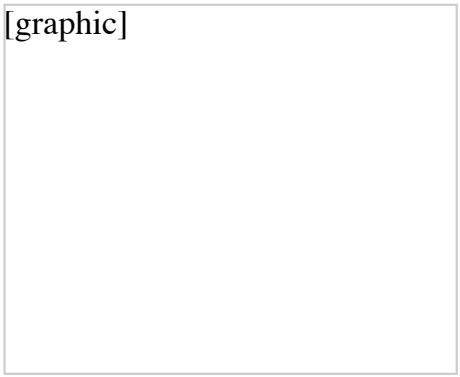

Fig. 76 Alloy 7075-T7352 forging, solution heat treated, cold reduced, and artificially aged. Particles are insoluble $(Fe,Mn)Al_6$ (dark gray). Some unresolved Mg_2Si may be present. This is a normal structure. See also Fig. 77. Keller's reagent. 250×

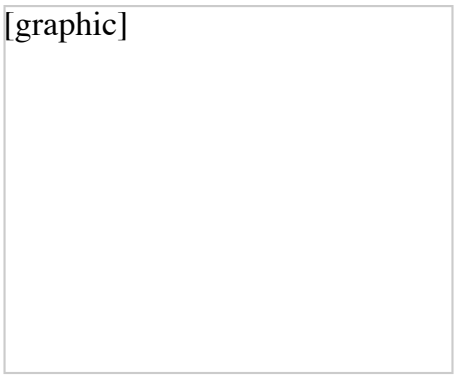

Fig. 77 Same alloy and condition as Fig. 76, but eutectic melting temperature was exceeded during solution heat treatment. Fusion voids (black areas) and agglomeration of insoluble phases (dark gray). Keller's reagent. 250×

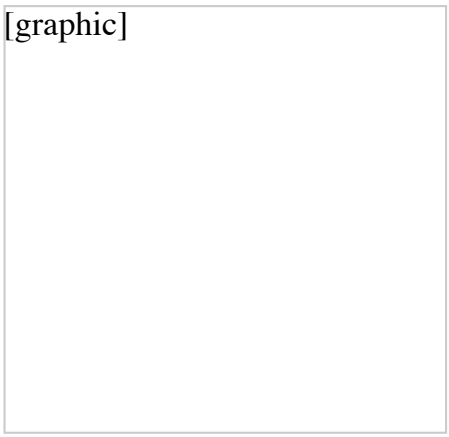

Fig. 78 Alloy 7075-T6 sheet clad with 0.07 mm (0.0027 in.) of alloy 7072 for 1.6-mm (0.064-in.) total thickness. Particles in cladding (top) are Fe_3SiAl_{12}; those in core are $Cr_2Mg_3Al_{18}$ and $(Fe,Mn)Al_6$. Keller's reagent. 350×

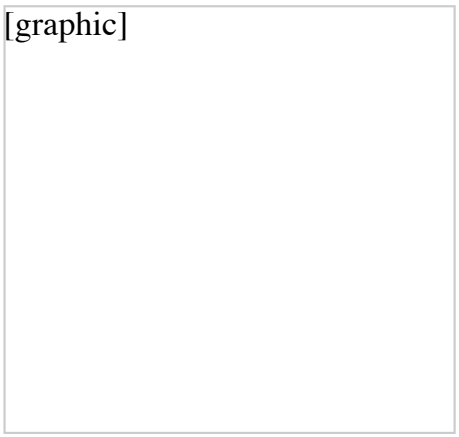

Fig. 79 Alloy 7178-T76 sheet, 3.2 mm (0.125 in.) thick, exposed in a test chamber containing a fog of 5% NaCl for two weeks. Note exfoliation of the sheet. See also Fig. 80. Keller's reagent. 75×

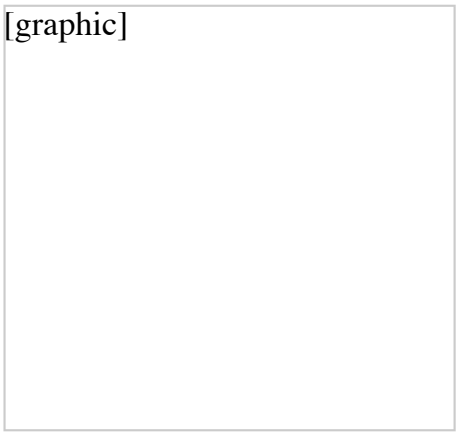

Fig. 80 Same alloy as in Fig. 79, but clad with 0.127 mm (0.005 in.) of alloy 7072 (3.2-mm, or 0.125-in. total thickness). Sacrificial corrosion of cladding prevented exfoliation of sheet during testing. Keller's reagent. 75×

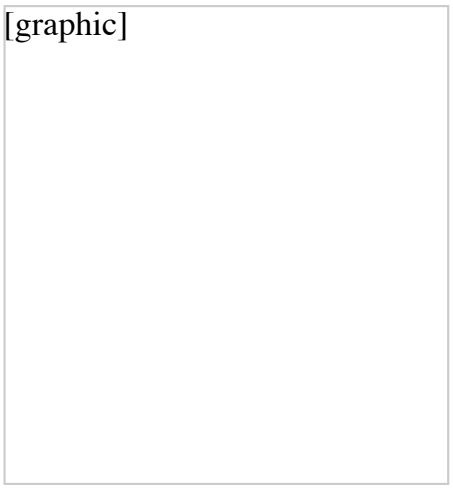

Fig. 81 Parting-plane fracture in an alloy 7075-T6 forging that contained a bushing in a machined hole. Fracture was caused by excessive assembly stress. See also Fig. 82 and 83. Keller's reagent. 1.5×. (J.M. Van Orden, E. Walden)

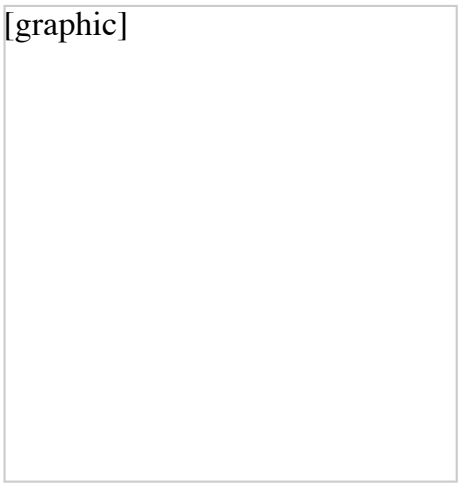

Fig. 82 Detail of parting-plane fracture in Fig. 81. The fracture started at the machined hole and progressed parallel to the flow lines of the forging. See also Fig. 83. Keller's reagent. 8×. (J.M. Van Orden, E. Walden)

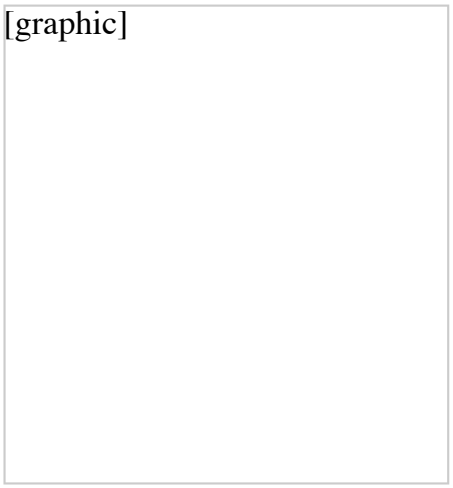

Fig. 83 Fracture surface of parting-plane fracture in Fig. 81 (machined hole at bottom). Woody, brittle fracture pattern is typical of parting-plane fracture in this alloy. Not polished, not etched. 4×. (J.M. Van Orden, E. Walden)

[graphic]

Fig. 84 Fold, or lap, at a machined fillet in a 7075-T6 forging. Defect was continuous before machining. See also Fig. 85 for details of a small area of the portion of the defect at lower right. Keller's reagent. 8×. (J.M. Van Orden, E. Walden)

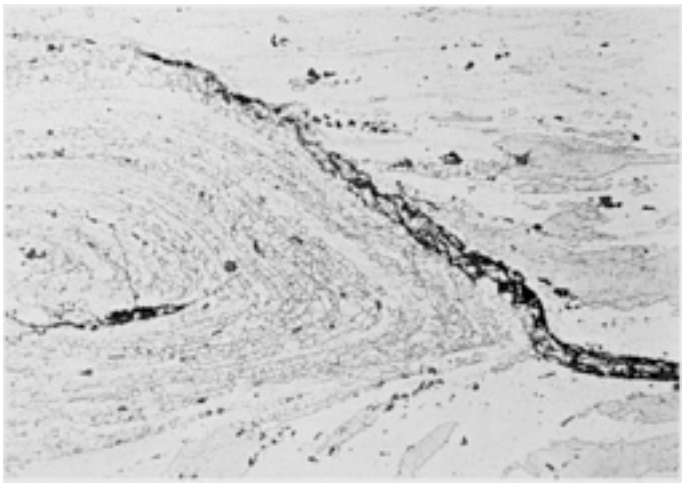

Fig. 85 Enlarged view of an area of the fold, or lap, at lower right in Fig. 84. Defect contains nonmetallic particles, oxides, and voids, which prevented it from welding, or healing, during forging. Keller's reagent. 200×. (J.M. Van Orden, E. Walden)

[graphic]

Fig. 86 Surface appearance of a lap (at trough, center) in an alloy 7075-T6 forging. Forging flow lines bend in the vicinity of the lap, indicating that the defect occurred during forging. See also Fig. 87. Not polished, not etched. 10×. (J.M. Van Orden, E. Walden)

[graphic]

Fig. 87 Section through the forging lap shown in surface view in Fig. 86. The trough at the surface is at the left. The grains near the lap are deformed, which indicates that the defect occurred during forging. Keller's reagent. 500×. (J.M. Van Orden, E. Walden)

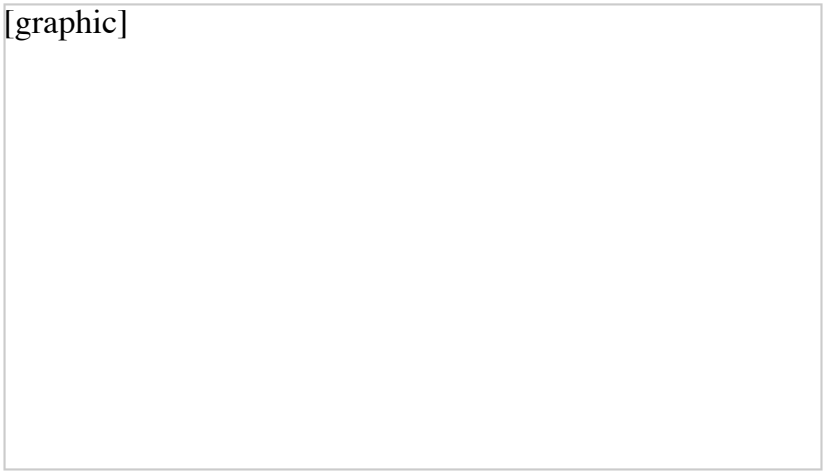

Fig. 88 Band of shrinkage cavities and internal cracks in an alloy 7075-T6 forging. The cracks developed from the cavities, which were produced during solidification of the ingot and which remained during forging because of inadequate cropping. See Fig. 90 and 92 for higher magnification views of this defect. Keller's reagent. 9×. (J.M. Von Orden, E. Walden)

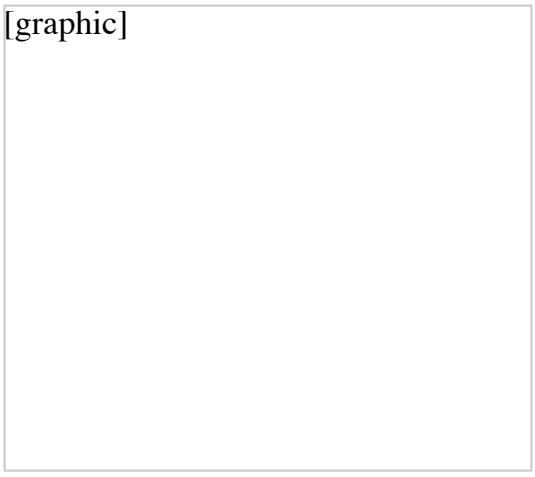

Fig. 89 Fractured lug of an alloy 7075-T6 forging. Arrows illustrate sites at machined hole where stress-corrosion cracks originated because of stress acting across the short transverse grain direction. See also Fig. 91. Keller's reagent. 2.75×. (J.M. Van Orden, E. Walden)

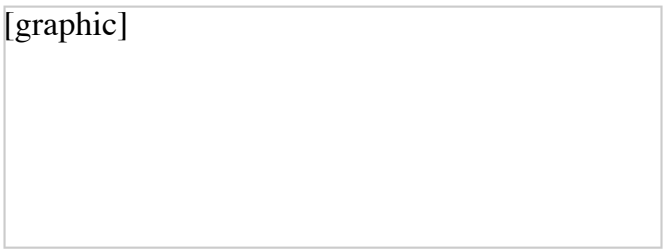

Fig. 90 Area of the forging in Fig. 88 that contains rows of unhealed shrinkage cavities (black), shown at higher magnification. No cracks have developed from the cavities in this particular area. See Fig. 92 for view of cracked area. Keller's reagent. 200×. (J.M. Van Orden, E. Walden)

Fig. 91 Higher magnification view of area of the fractured lug in Fig. 89 that contains intergranular cracks caused by stress corrosion, which resulted when assembly of a pin in the machined hole produced excessive residual hoop stress in the lug. Keller's reagent. 200×. (J.M. Van Orden, E. Walden)

Fig. 92 Area of the forging in Fig. 88 that contains intergranular and connecting transgranular cracks shown at a higher magnification. The cracks developed from shrinkage cavities. See also Fig. 90. Keller's reagent. 200×. (J.M. Van Orden, E. Walden)

Fig. 93 Brittle fracture surfaces in a tension-test specimen machined from an alloy 7075-T6 forging that contained a defect of the type shown in Fig. 88 (shrinkage cavities and internal cracks). Not polished, not etched. 3×. (J.M. Van Orden, E. Walden)

Fig. 94 Fracture in an alloy 7075-T6 extrusion, showing segregation of chromium particles (light gray, fractured). Segregation originated in the ingot and persisted through to the final product. Keller's reagent. 200×. (J.M. Van Orden, E. Walden)

Fig. 95 Fracture in an alloy 7075-T6 extrusion, showing a spongy inclusion of dross (center) and some segregation of chromium particles (left) at fracture surface, both of which originated in the ingot. Keller's reagent. 200×. (J.M. Van Orden, E. Walden)

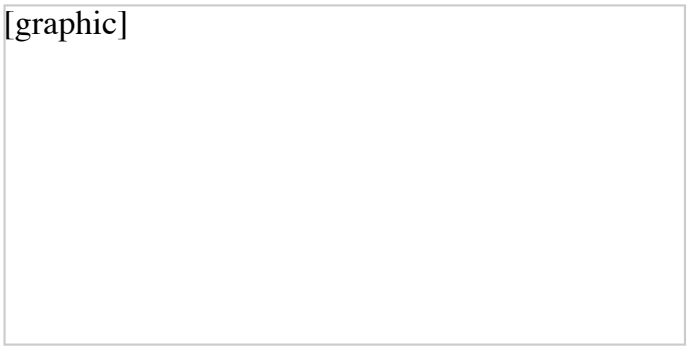

Fig. 96 Pitting-type corrosion (dark area) in the surface of an aircraft-wing plank machined from an alloy 7075-T6 extrusion. Keller's reagent. 200×. (J.M. Van Orden, E. Walden)

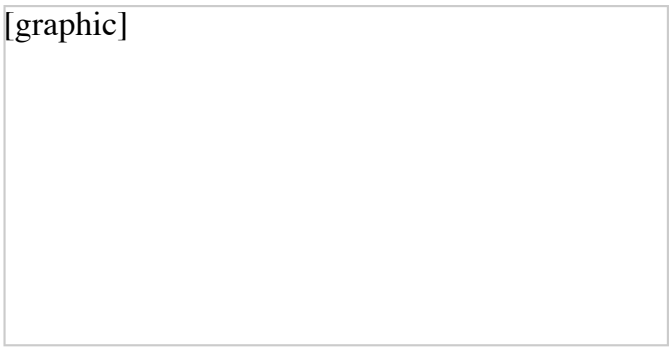

Fig. 97 Intergranular corrosion in alloy 7075-T6 plate. Grain boundaries were attacked, causing the grains to separate. Keller's reagent. 200×. (J.M. Van Orden, E. Walden)

Fig. 98 Exfoliation-type corrosion in an alloy 7075-T6 extrusion. Rapid attack was parallel to the surface of the extrusion and along the grain boundaries or along striations within elongated grains. See also Fig. 99. Keller's reagent. 20×. (J.M. Van Orden, E. Walden)

Fig. 99 Higher magnification view of Fig. 98 (rotated 90°), showing how the corrosion product caused the uncorroded, recrystallized skin of the extrusion to split away, resulting in a leafing action. Keller's reagent. 200×. (J.M. Van Orden, E. Walden)

[graphic]

Fig. 100 Typical ductile fracture in alloy 7075-T6 alclad sheet, showing the deformed grains and necking at the fracture. Keller's reagent. 200×. (J.M. Van Orden, E. Walden)

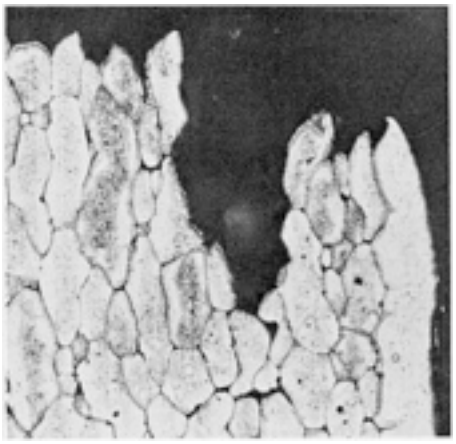

Fig. 101 Brittle fracture in overheated alloy 7075-T6 alclad sheet, caused by solid-solution melting at the grain boundaries. Keller's reagent. 200×. (J.M. Van Orden, E. Walden)

[graphic]

Fig. 102 Typical branched intergranular stress-corrosion cracks in an alloy 7075-T6 extruded bar. Transverse section. Keller's reagent. 200×. (J.M. Van Orden, E. Walden)

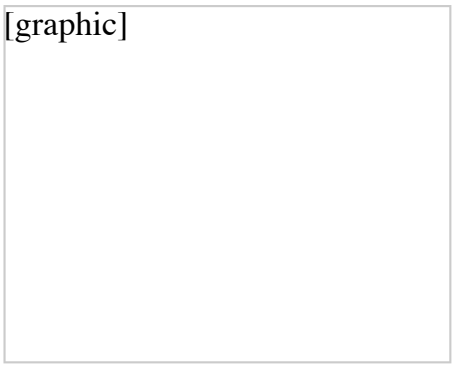

Fig. 103 Alloy 222-T61, sand cast, solution heat treated, and artificially aged. The structure consists of an interdendritic network of rounded $CuAl_2$ containing blades of Cu_2FeAl_7, and some Fe_3-$SiAl_{12}$ (dark-gray script). 0.5% HF 250×

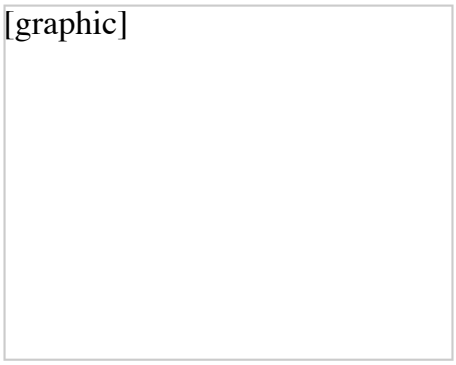

Fig. 104 Alloy 238-F, as permanent mold cast. The structure consists of an interdendritic network of rounded $CuAl_2$ (light gray) containing blades of Cu_2FeAl_7 (medium gray), and some particles of silicon (dark gray). 0.5% HF. 500×

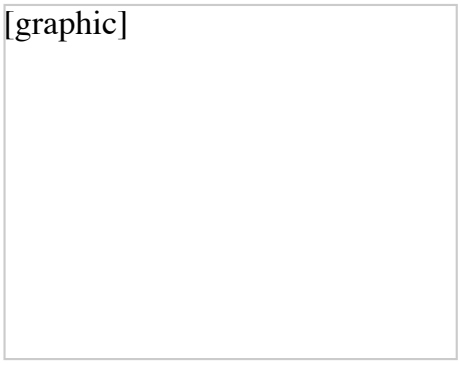

Fig. 105 Alloy A240-F, as investment cast. The microstructure contains large shrinkage voids (black), an interdendritic network of Al-Cu-Mg eutectic (mottled), and some interdendritic particles of $CuMgAl_2$ (gray). As-polished. 50×

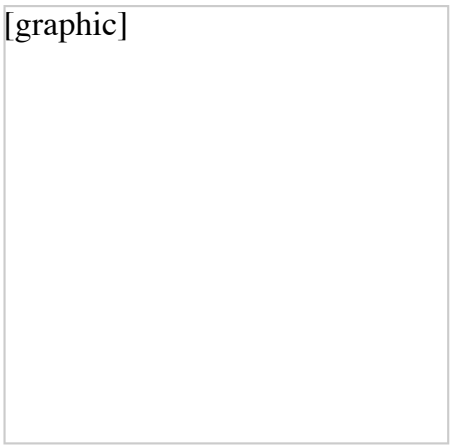

Fig. 106 Alloy 242-F, as permanent mold cast. Structure consists of interdendritic network of particles of $CuAl_2$ (light, speckled), Cu_3NiAl_6 (medium-gray script), $NiAl_3$ (dark-gray blades), and Mg_2Si (black script). 0.5% HF. 100×

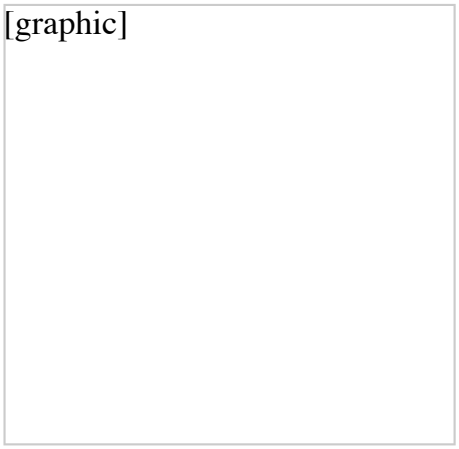

Fig. 107 Alloy 242-T571, permanent mold cast and artificially aged. Structure contains blades of $NiAl_3$ (dark gray) in the medium-gray Cu_3NiAl_6 script. $CuAl_2$ particles (light) and scriptlike Mg_2Si (black) also are present. 0.5% HF. 250×

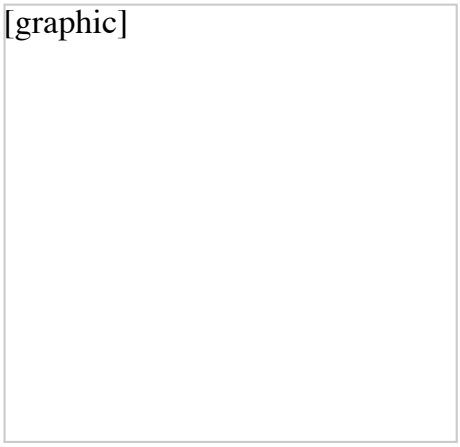

Fig. 108 Alloy 242-T77, sand cast and heat treated. Constituents are the same as Fig. 107, but particles of $NiAl_3$ and Cu_3NiAl_6 have been rounded by solution heat treatment. Precipitation is caused by overaging treatment. 0.5% HF. 250×

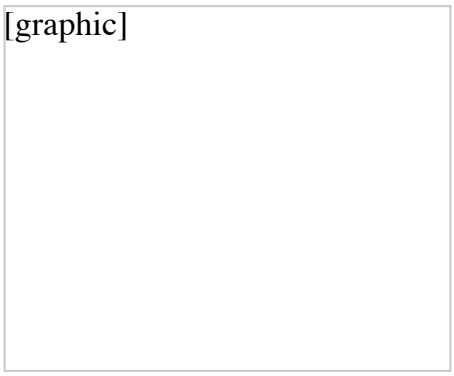
[graphic]

Fig. 109 Alloy A332-F, as investment cast. Interdendritic network of eutectic silicon (medium-gray script), Mg_2Si (black script), Cu_3NiAl_6 (light-gray script), and $NiAl_3$ (dark-gray particles). See also Fig. 110 and 111. 0.5% HF. 250×

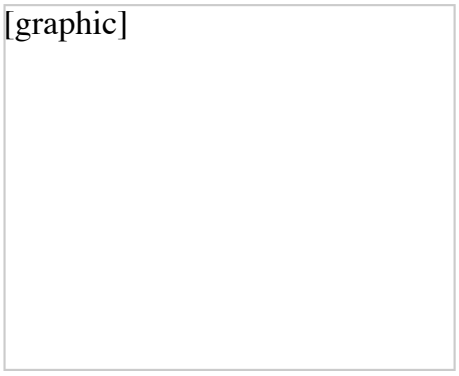
[graphic]

Fig. 110 Alloy A332-T551, sand cast and artificially aged. Constituents are same as those of the structure in Fig. 109; but there is less Cu_3NiAl_6, and the particles of $NiAl_3$ are more massive. See also Fig. 111. 0.5% HF. 250 ×

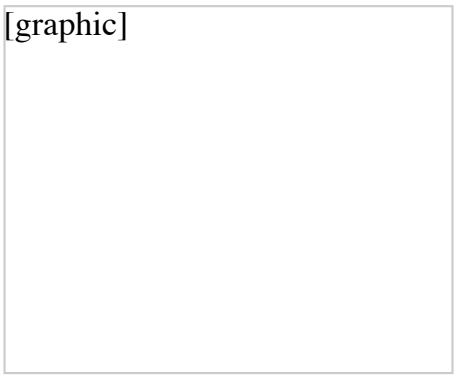
[graphic]

Fig. 111 Alloy A332-T65, sand cast, solution heat treated, and artificially aged. Constituents are same as in Fig. 109, but the particles of silicon in the eutectic have been made more rounded by the solution heat treatment. 0.5% HF. 250×

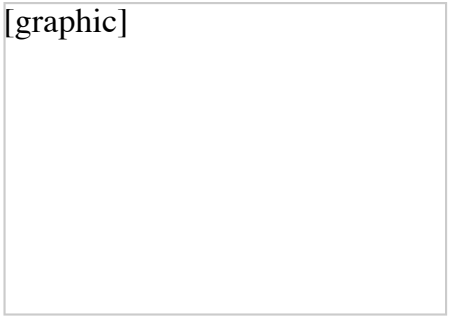
[graphic]

Fig. 112 Alloy 354-F, as investment cast. Structure consists of a network of silicon particles (dark

gray, angular) in a divorced interdendritic aluminum-silicon eutectic and particles of $Cu_2Mg_8Si_6Al_5$ phase (light gray, scriptlike). 0.5% HF. 250×

[graphic]

Fig. 113 Alloy 354-F, as investment cast with two chills adjacent to the area shown. Constituents are the same as for Fig. 112; but dendritic cells are finer, and silicon particles in eutectic are smaller and less angular. 0.5% HF. 250×

[graphic]

Fig. 114 A 354-T4 investment casting with fusion voids (black) caused by eutectic melting when solidus was exceeded in solution heat treatment. Surface of casting is blistered. Gray particles are eutectic silicon. 0.1% HF. 50×

[graphic]

Fig. 115 Alloy 355-F, as investment cast. Structure consists of an interdendritic network of eutectic silicon (dark gray, sharp), $Cu_2Mg_8Si_6Al_5$ (light-gray script), $Fe_2Si_2Al_9$ (medium-gray blades), and Mg_2Si (black, at left). 0.5% HF. 250×

[graphic]

Fig. 116 Alloy 355-F modified by the addition of Al-10Sr alloy to the melt, as investment cast. Constituents are the same as in Fig. 115, but the particles of silicon (dark gray) are less sharply angular. 0.5% HF. 250×

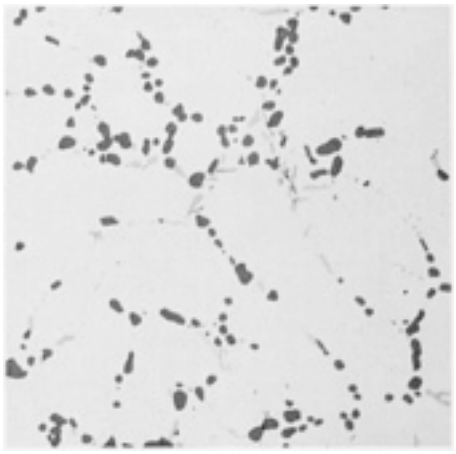

Fig. 117 Alloy 355-T6, permanent mold cast, solution heat treated, and artificially aged. Constituents are the same as in Fig. 115, but eutectic silicon particles have been rounded by the solution heat treatment. 0.5% HF. 500×

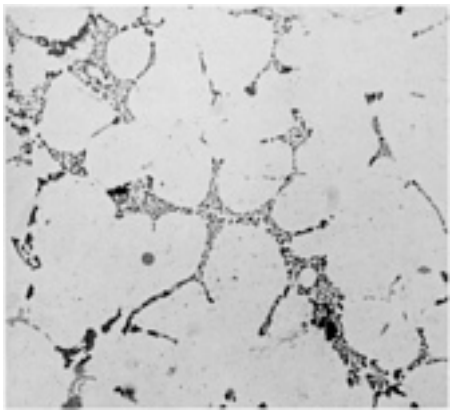

Fig. 118 Alloy 356-F, as investment cast with sodium-modified ingot. Interdendritic structure: particles of silicon (dark gray), $FeMg_3Si_6Al_8$ (light-gray script), $Fe_2Si_2Al_9$ (medium-gray blades), and Mg_2Si (black). 0.5% HF. 250×

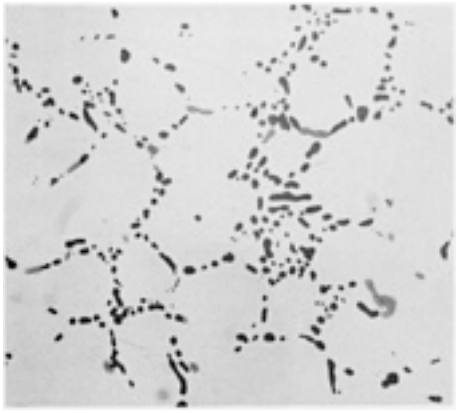

Fig. 119 Alloy 356-T6, investment cast with sodium-modified ingot, solution heat treated, artificially aged. Solution treatment has rounded and agglomerated the particles of silicon, compared with those in Fig. 118. 0.5% HF. 250×

[graphic]

Fig. 120 Alloy 356-T6, investment cast in a hot mold (650 °C, or 1200 °F) and heat treated. Inverse coring, large dendrite-arm spacing, and large particles of silicon that resulted from the slow cooling; also, shrinkage cavities. Keller's reagent. 50×

[graphic]

Fig. 121 Alloy 356-F, as sand cast. Structure consists of a network of silicon particles (gray, sharp), which formed in the interdendritic aluminum-silicon eutectic. See also Fig. 122 and 123. 0.5% HF. 100×

[graphic]

Fig. 122 Alloy 356-T4, sand cast, solution heat treated at 540 °C (1000 °F) for 12 h, quenched in boiling water. Heat treatment caused silicon particles to be rounder than in Fig. 121 (as-cast). 0.5% HF. 100×

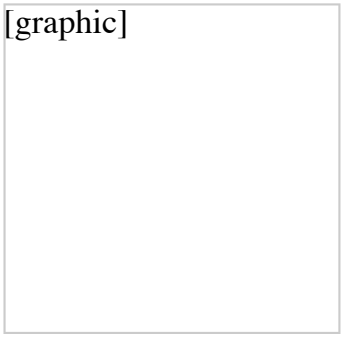

Fig. 123 Alloy 356-F, modified by addition of 0.025% Na to the melt, as sand cast. Constituents same as for Fig. 121, but the particles of silicon in the eutectic are smaller and less angular. 0.5% HF. 100×

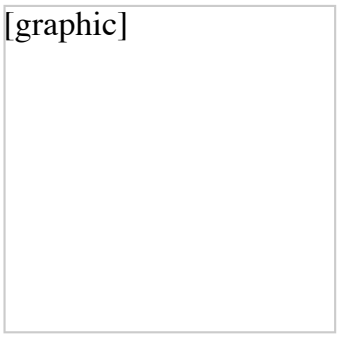

Fig. 124 Alloy 356-T4, modified by addition of 0.025% Na, sand cast and heat treated as described in Fig. 122. Silicon particles are rounded and agglomerated. See also Fig. 121, 122, and 123. 0.5% HF 100×

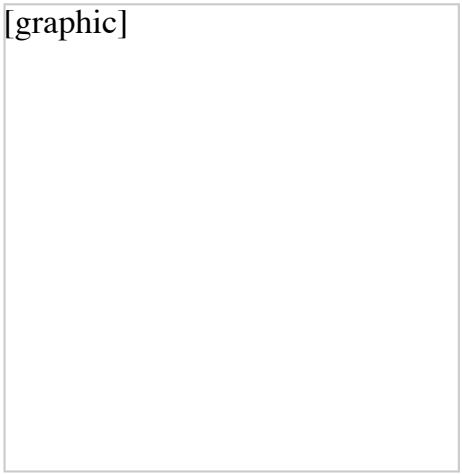

Fig. 125 Alloy 356-T51, sand cast, artificially aged. The angular, dark gray constituent is silicon. Black script is Mg_2Si. Blades are $Fe_2Si_2Al_9$. Light script is $FeMg_3Si_6Al_8$. 0.5% HF. 250×

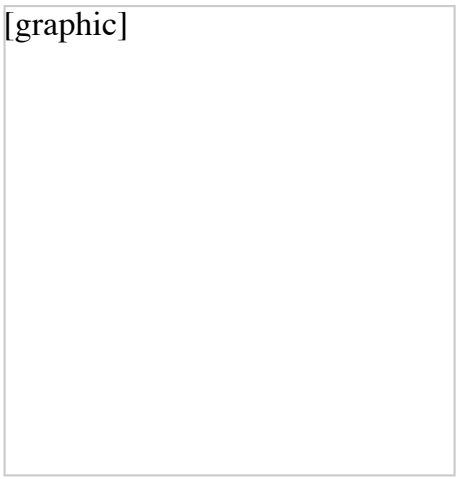
[graphic]

Fig. 126 Alloy 356-T7, modified by sodium addition, sand cast, solution heat treated, and stabilized. Structure: rounded particles of silicon and blades of $Fe_2Si_2Al_9$. 0.5% HF. 250×

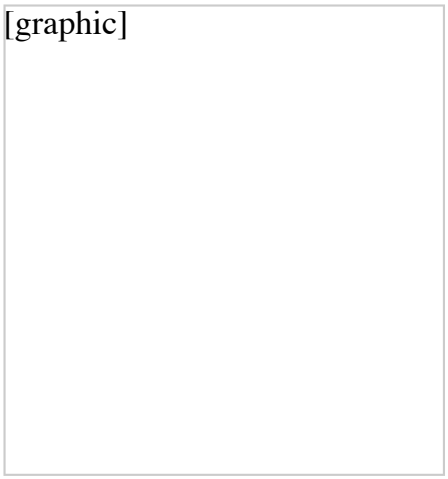
[graphic]

Fig. 127 Al_2O_3 inclusions (black) in alloy 356-F, as investment cast with sodium-modified ingot. Light gray interdendritic network consists of particles of silicon. As-polished. 50×

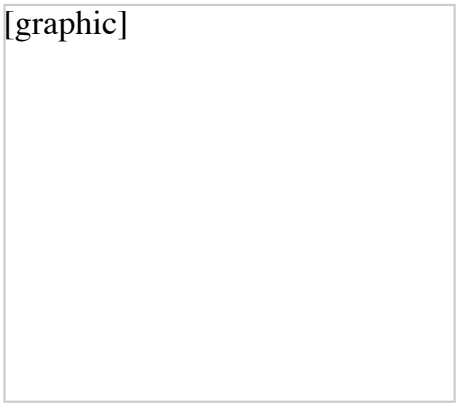
[graphic]

Fig. 128 Hydrogen porosity (black) in a 356-T6 permanent mold casting that had been solution heat treated and artificially aged. 0.5% HF. 100×

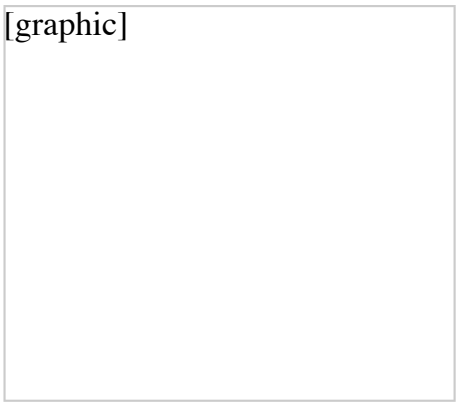
[graphic]

Fig. 129 Alloy A356-F sand casting to which no grain refiner was added. The macrograin size is 5 mm (0.20 in.). See also Fig. 130. Tucker's reagent. 2×

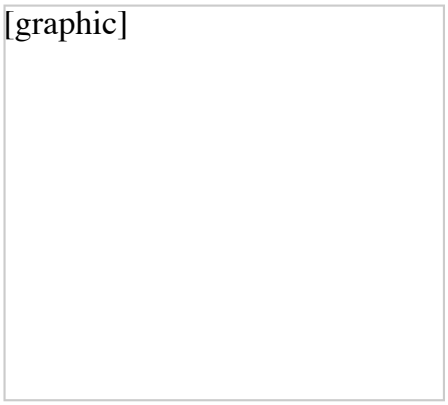
[graphic]

Fig. 130 Alloy A356-F sand casting with 0.05% Ti and 0.005% B added as grain refiners. Macrograin size is 1 mm (0.04 in.). Tucker's reagent. 2×

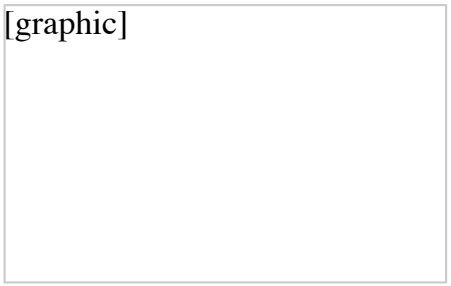
[graphic]

Fig. 131 Alloy A357-T61, permanent mold cast, solution heat treated at 540 °C (1000 °F) for 12 h, quenched in water at 60 to 80 °C (140 to 180 °F), aged at 155 °C (310 °F) for 10 h. A desirable structure: rounded silicon particles and no undissolved Mg_2Si. See also Fig. 132. 0.5% HF. 500×

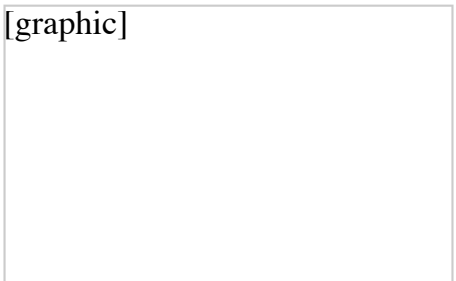
[graphic]

Fig. 132 Alloy A357-T61, permanent mold cast, insufficiently solution heat treated and artificially aged. Structure contains undissolved Mg_2Si (black), and some of the particles of silicon are more angular than those in the desirable structure shown in Fig. 131. 0.5% HF. 500×

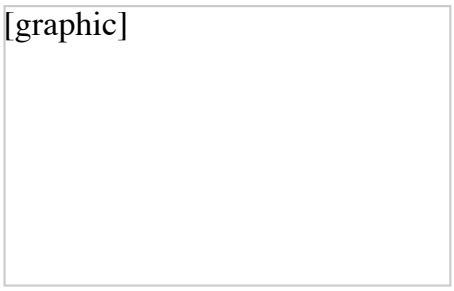

Fig. 133 Alloy 413-F, as die cast. The structure consists of eutectic silicon (gray constituent), blades of $Fe_2Si_2Al_9$, and some light-gray particles that probably are Fe_3SiAl_{12} in a matrix of aluminum solid solution. Note extreme fineness of all particulate constituents. 0.5% HF. 100×

Fig. 134 Alloy 392-F, as permanent mold cast. The structure consists of silicon (small, angular, gray particles in eutectic, and large, unrefined primary particles) and Mg_2Si (black constituent). See also Fig. 135. 0.5% HF. 100×

Fig. 135 Alloy 392-F, as permanent mold cast same as for Fig. 134, but phosphorus was added to the melt. This addition refined the size of the particles of primary silicon. 0.5% HF. 100×

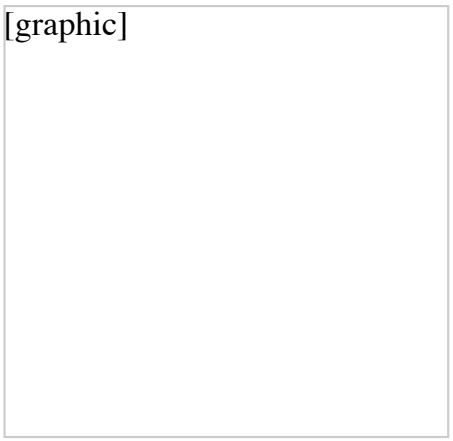

Fig. 136 Alloy 443-F, as sand cast. Large dendrite cells resulted from slow cooling in the sand mold. Interdendritic structure: silicon (dark gray), Fe_3SiAl_{12} (medium gray script), and $Fe_2Si_2Al_9$ (light gray needles). 0.5% HF. 500×

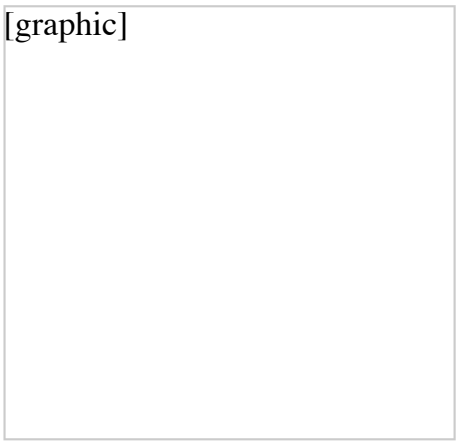

Fig. 137 Alloy B443-F, as permanent mold cast. The constituents are the same as those in Fig. 136 (a sand casting), but dendrite cells are smaller because of faster cooling in the metal permanent mold. See also Fig. 138. 0.5% HF. 500×

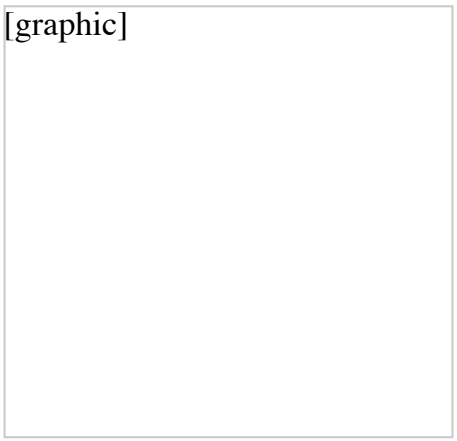

Fig. 138 Alloy C443-F, as die cast, Same constituents as in Fig. 136 and Fig. 137, but dendrite cells are smaller because of the very rapid cooling obtained in the water-cooled die-casting die. 0.5% HF. 500×

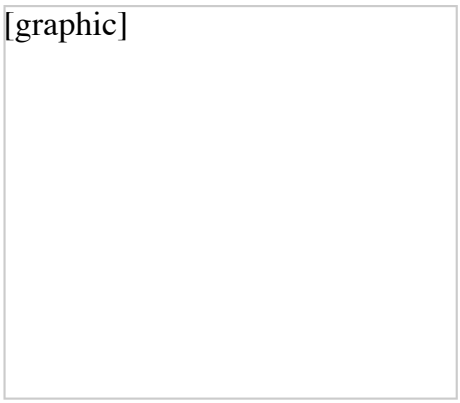

Fig. 139 Alloy 308-F, as permanent mold cast. Structure consists of an interdendritic network of silicon particles (dark gray, angular) and rounded particles of $CuAl_2$ (light gray) that contain blades of $Fe_2Si_2Al_9$. 0.5% HF. 250×

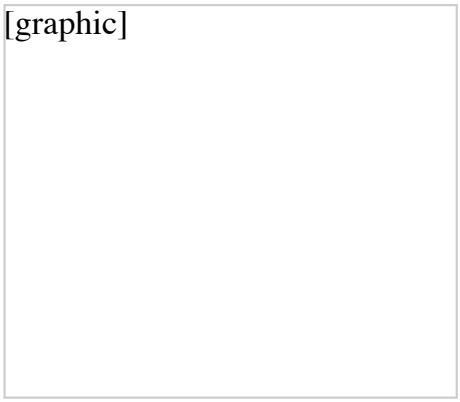

Fig. 140 Alloy 319-F, as permanent mold cast. Dendrites of aluminum solid solution show segregation (coring). Other constituents are interdendritic network of silicon (dark gray) rounded $CuAl_2$, and $(Fe,Mn)_3SiAl_{12}$ script. Keller's reagent. 100×

Fig. 141 Alloy 319-T6, permanent mold cast, solution heat treated, and artificially aged. Segregation in dendrites of solid solution was eliminated by diffusion, and $CuAl_2$ was dissolved during solution heat treating. Keller's reagent. 100×

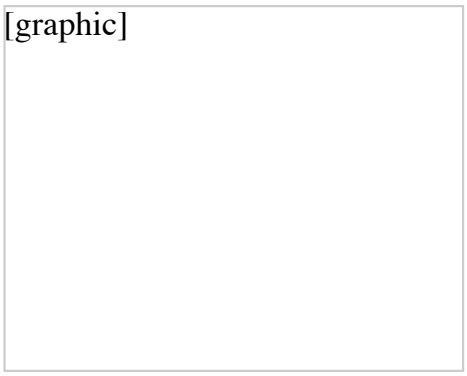

Fig. 142 Alloy 520-F, as sand cast. Structure is insoluble particles of $FeAl_3$ (black) and an interdendritic network of Mg_2Al_3 phase (gray). See Fig. 143 and 144 for the effect of solution heat treatment. 0.5% HF. 100×

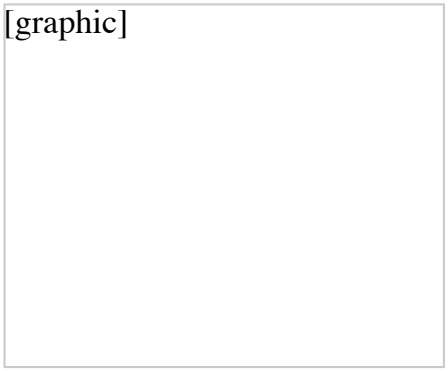

Fig. 143 Alloy 520-T4, sand cast, solution heat treated at 425 °C (800 °F). Constituents are the same as in Fig. 142, but the solution heat treating has dissolved most of the Mg_2Al_3 phase (gray). See also Fig. 144. 0.5% HF. 100×

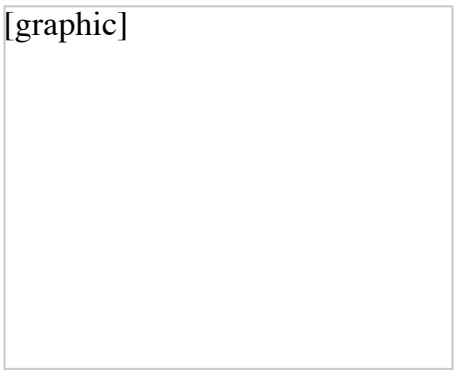

Fig. 144 Alloy 520-T4, sand cast, solution heat treated. Solidus was exceeded during solution heat treating, and melting of the eutectic has formed a lacy network and rosettes of Mg_2Al_3 phase (gray). See also Fig. 143. 0.5% HE 500×

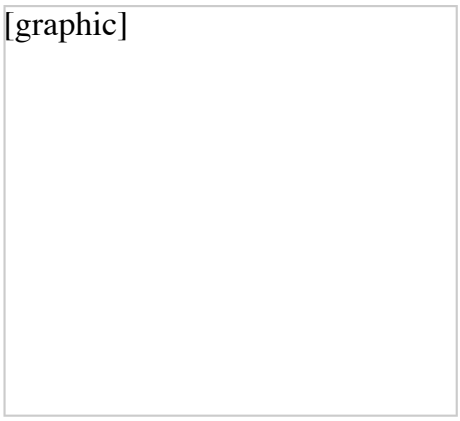

Fig. 145 Alloy D712-F, as sand cast. Interdendritic network: particles of $CrAl_7$, Fe_3SiAl_{12}, and $FeAl_6$. Note the segregation (coring) of magnesium and zinc in the grains. See also Fig. 146. Keller's reagent. 100×

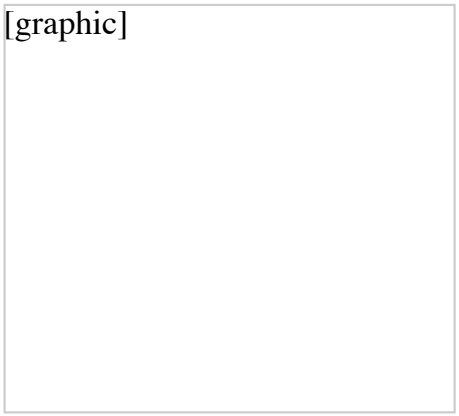

Fig. 146 Alloy D712-F, as investment cast. Same constituents as in Fig. 145. Intergranular fusion voids (black) were caused by eutectic melting as a result of exceeding the solidus temperature during dip brazing, Keller's reagent. 100×

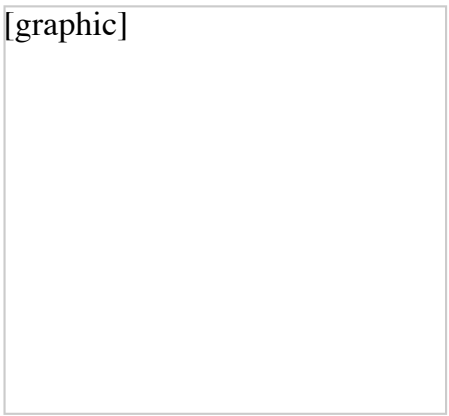

Fig. 147 Alloy 850-F, as permanent mold cast. Note hot tear, which occurred at or above the solidus, and some Al-$CuAl_2$ eutectic (gray) back filling of tear. Particles of tin (rounded), $NiAl_3$, and $FeNiAl_9$ (both irregular). 0.5% HF. 100×

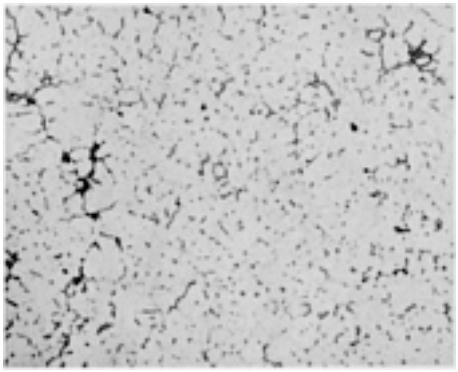

Fig. 148 Alloy 201-F, as premium quality cast. Structure consists of an interdendritic network of undissolved eutectic $CuAl_2$ (gray, outlined); some shrinkage cavities (black). See Fig. 149 and 150 for the effect of solution heat treatment and stabilization. 0.5% HF. 100×

[graphic]

Fig. 149 Alloy 201-T7, premium quality cast, solution heat treated, and stabilized. Structure is a fine precipitate of $CuAl_2$ in grains and at grain boundaries; no undissolved eutectic $CuAl_2$; some shrinkage cavities (black). See Fig. 150 for structure at higher magnification. 0.5% HF. 100×

[graphic]

Fig. 150 Higher magnification view of Fig. 149 showing the pattern of $CuAl_2$ precipitate that resulted from segregation of copper (coring). Note that the presence of silver in the alloy has resulted in some agglomeration of the precipitate. See also Fig. 153. 0.5% HF. 500×

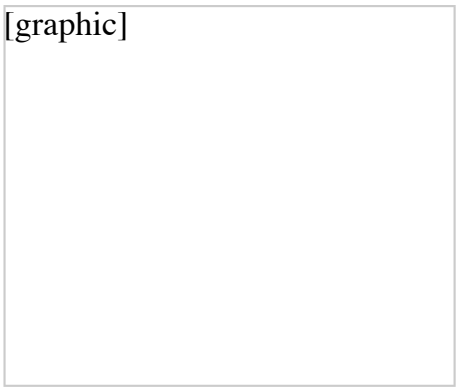

Fig. 151 Alloy 224-F, as premium quality cast. The structure consists of an interdendritic network of undissolved eutectic $CuAl_2$ (gray, outlined). See Fig. 152 and 153 for the effect of heat treatment on the structure. 0.5% HF. 100×

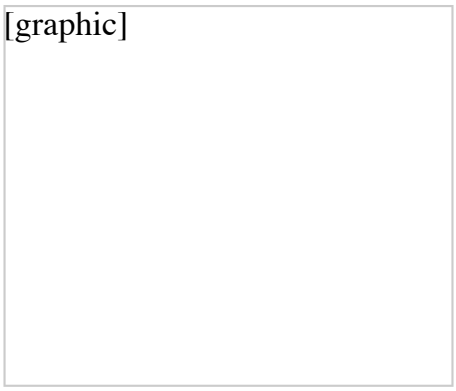

Fig. 152 Alloy 224-T7, premium quality cast, solution heat treated, and stabilized. Structure: fine $CuAl_2$ precipitate; almost all of the eutectic $CuAl_2$ present in Fig. 151 has been dissolved. See also higher magnification view in Fig. 153. 0.5% HF. 100×

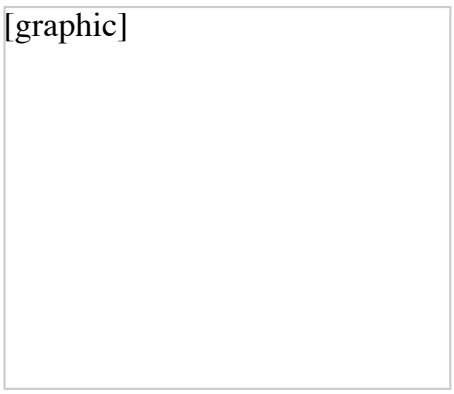

Fig. 153 Enlarged view of structure in Fig. 152 showing a fairly even pattern of very fine particles of $CuAl_2$ precipitate in the aluminum grains and slightly larger particles of the precipitate at grain boundaries. 0.5% HF. 500×

[graphic]

Fig. 154 Alloy A357-F, as premium quality cast. The structure consists of an interdendritic network of eutectic silicon (gray); some particles of Mg_2Si (black). See Fig. 155 and 156 for the effect of solution heat treatment and artificial aging. 0.5% HF. 100×

[graphic]

Fig. 155 Alloy A357-T6, premium quality cast, solution heat treated, and artificially aged. Compared with Fig. 154, the silicon particles in the eutectic have been rounded and agglomerated by solution heat treatment. See Fig. 156 for a higher magnification view. 0.5% HF. 100×

[graphic]

Fig. 156 Structure in Fig. 155 at higher magnification, which shows that very little undissolved Mg_2Si (black particles) remained after solution heat treatment. No silicon precipitate is visible. See Fig. 132 for the effect of insufficient solution heat treatment. 0.5% HF. 500×

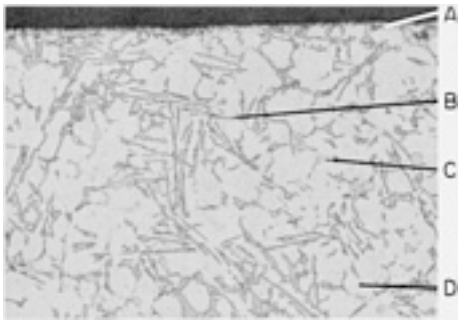

Fig. 157 Alloy 380-F die casting. Area near a machined surface (A) shows structure typical of a casting that has desirable properties: interdendritic particles of eutectic silicon (B) and $CuAl_2$ (C) in a matrix of aluminum solid solution (D). See also Fig. 158. 0.5% HF. 260×. (G.L. Armstrong)

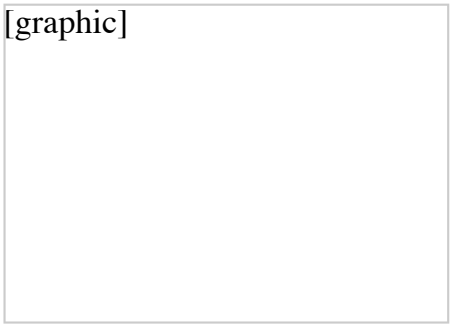

Fig. 158 Alloy 380-F die casting. Area near a machined surface (A) illustrates some primary crystals of sludge (B) in the aluminum matrix (C) that contains eutectic silicon (D). Sludge is a high-melting iron-manganese-chromium phase that forms in high-silicon aluminum alloys. 0.5% HF. See also Fig. 157. 130×. (G.L. Armstrong)

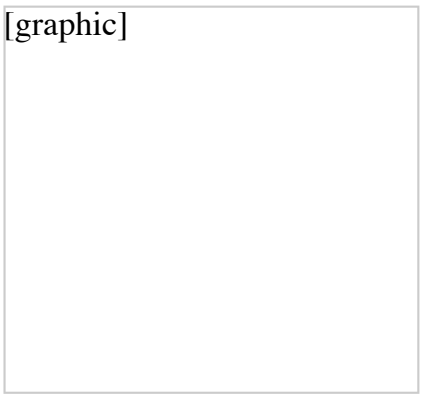

Fig. 159 Flow lines (A, B, and C) in an alloy 384-F die casting. These may have been caused by incorrect gating, incorrect die lubrication, or incorrect injection and back pressures. 0.5% HF. 65×. (G.L. Armstrong)

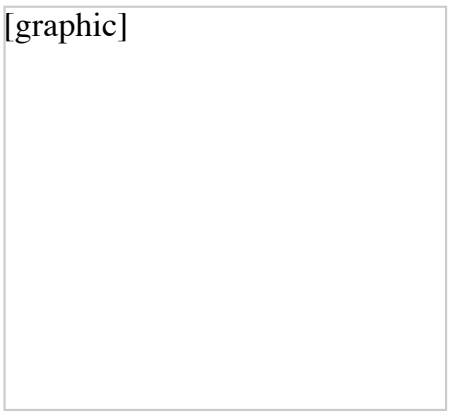

Fig. 160 Fine Al_2O_3 (A), which should not cause machining difficulties, near the machined surface (B) of an alloy 380-F die casting. Eutectic silicon is indicated by (C); $CuAl_2$ by (D), and sludge, by (E). See also Fig. 161. 0.5% HF. 260×. (G.L. Armstrong)

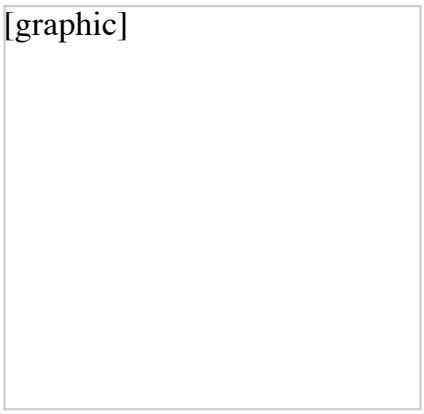

Fig. 161 Same material as Fig. 160, but at a higher magnification. Aluminum oxide particles are indicated by (A) and (B); particles of eutectic silicon, by (C); aluminum matrix, by (D); and particles of sludge, by (E). 0.5% HF. 520×. (G.L. Armstrong)

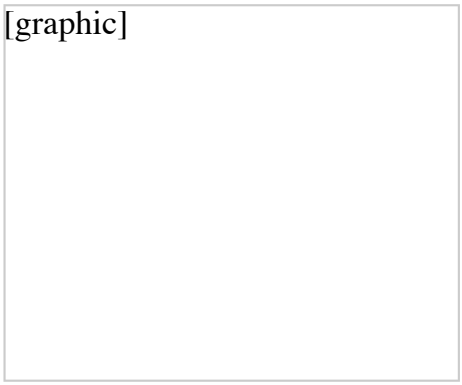

Fig. 162 Hard area (A) at a machined surface (B) of an alloy 380-F die casting. See Fig. 163 and 164 for details of the microstructure in the hard area, which differs from the normal microstructure (C). 0.5% HF. 65×. (G.L. Armstrong)

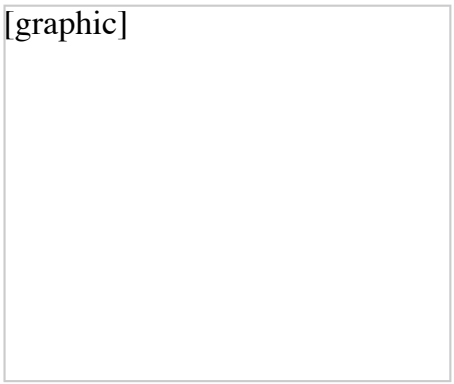

Fig. 163 Edge of hard area in Fig. 162 shown at a higher magnification. Hard area (A) is separated from the area of normal structure (B) by a "flow line" (C) where two streams of liquid alloy met. Some sludge (D) in hard area. 0.5% HF. 425×. (G.L. Armstrong)

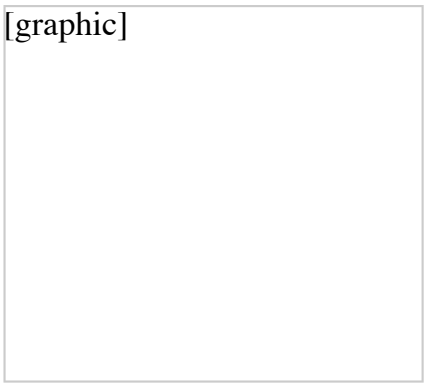

Fig. 164 Hard area in Fig. 162 shown at a higher magnification. Structure consists of a heavy concentration of eutectic silicon (A) and $CuAl_2$ (B) in the aluminum matrix (C). The hard area caused difficulty in machining. 0.5% HF. 1300×. (G.L. Armstrong)

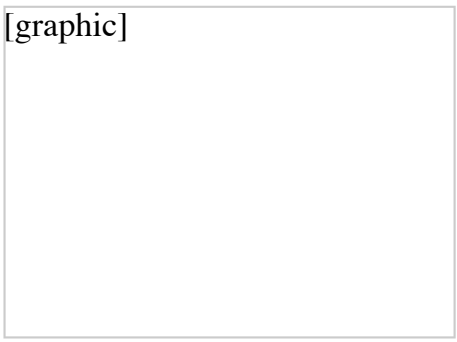

Fig. 165 Alloy 384-F die casting. Region near a cast surface (A) has the desired structure, which consists of interdendritic particles of eutectic silicon (B) in an aluminum matrix (C), but also has some Al_2O_3 particles (D, and in outlined area E). For a higher magnification view of area (E), see Fig. 166. 0.5% HF. 65×. (G.L. Armstrong)

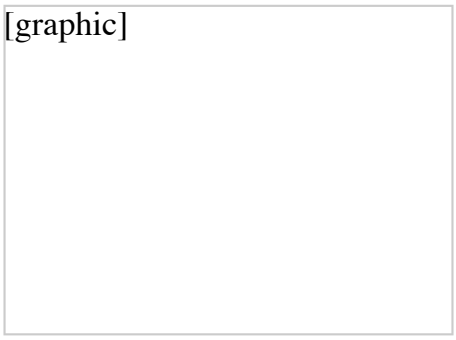

Fig. 166 Area (E) in Fig. 165 at higher magnification, which shows that the Al_2O_3 particles (A and B) are fine and may not cause machining problems. Small particles of sludge (C, D, and E) are associated with the Al_2O_3 particles. (F) is eutectic silicon; (G) is matrix of aluminum solid solution. 0.5% HF. 520×. (G.L. Armstrong)

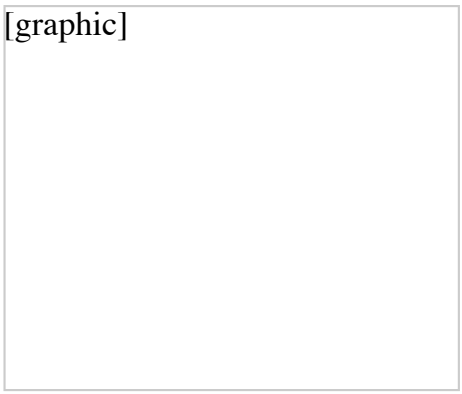
[graphic]

Fig. 167 Cold-shut voids (A, B) and flow lines (C, D), both caused by failure of the streams of molten metal to merge, at the cast surface (E) of an alloy 384-F die casting. 0.5% HF. 55×. (G.L. Armstrong)

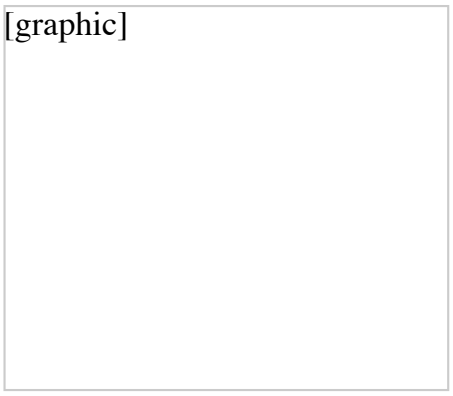
[graphic]

Fig. 168 Void (A), which was caused by poor filling of the mold and associated flow lines (B) in an alloy 384-F die casting. See Fig. 169 for flow lines without voids. 0.5% HF. 65×. (G.L. Armstrong)

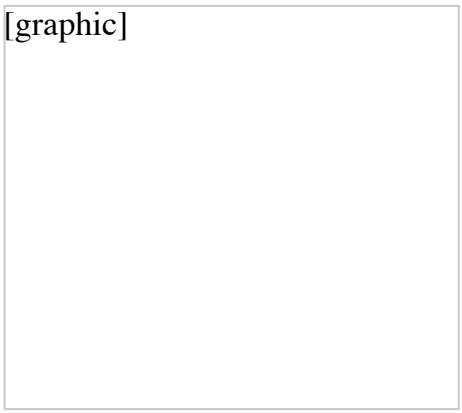
[graphic]

Fig. 169 Gas porosity (A), caused by entrapped air, near the machined surface (B) of an alloy 380-F die casting. Eutectic silicon particles (C) in aluminum matrix (D), and particles of sludge (E and F). 0.5% HF. 130×. (G.L. Armstrong)

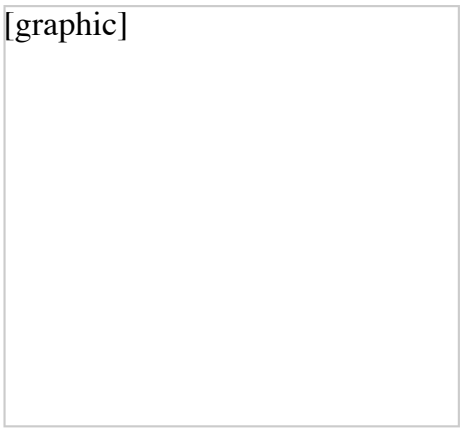

Fig. 170 Gas-porosity cavity (A), which was caused by entrapped air, at a machined surface (B) of an alloy 384-F die casting. Microstructure is eutectic silicon (C) in an aluminum matrix (D); some sludge (E) is present. 0.5% HF. 130×. (G.L. Armstrong)

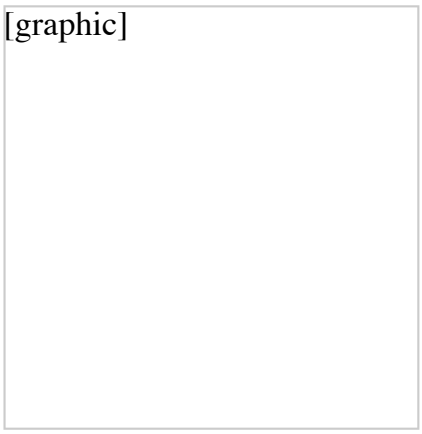

Fig. 171 Coarse primary crystals of sludge (A, B, C, and D) removed from molten alloy 384 prior to die casting. The remainder of the structure consists of aluminum matrix (E), eutectic silicon (F), and Al_2O_3 (G). 0.5% HF. 40×. (G.L. Armstrong)

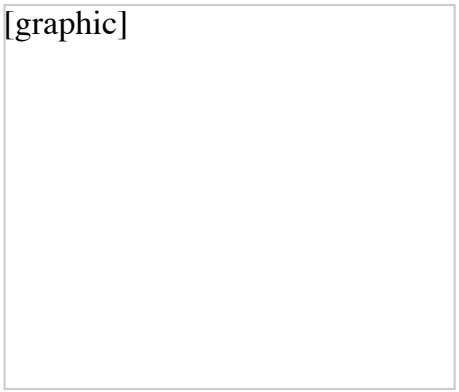

Fig. 172 Alloy 413-F die casting. The gate area (A) of the casting has the desired structure, which consists of interdendritic particles of eutectic silicon (B) and the light-etching matrix of aluminum solid solution (C). 0.5% HF. 41×. (G.L. Armstrong)

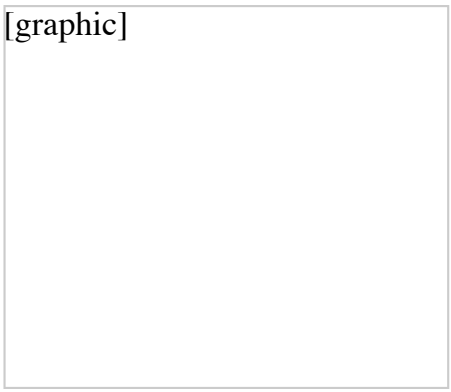
[graphic]

Fig. 173 Gate area (A) of an alloy 413-F die casting, showing gas porosity (B, C, and D) scattered from the outside wall (E) to the inside wall (F). See Fig. 174 for details of (G), a sound region. 0.5% HF. 11×. (G.L. Armstrong)

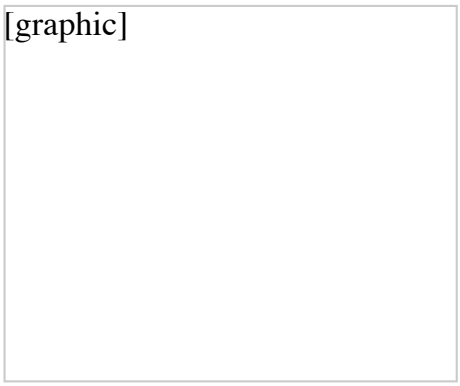
[graphic]

Fig. 174 Area (G) in Fig. 173 at a higher magnification. Angular eutectic silicon (A) in matrix of aluminum solid solution (B) in normal structure and rounded silicon in undesirable structures (C and D). 0.5% HF. 520×. (G.L. Armstrong)

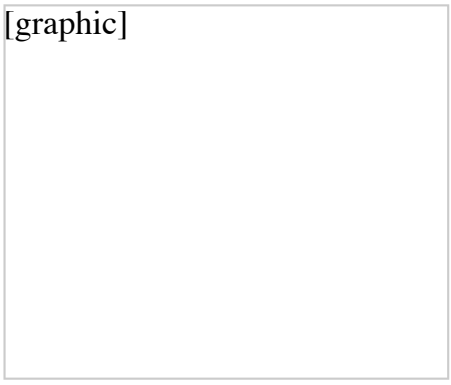
[graphic]

Fig. 175 Gate area (A) of an alloy 413-F die casting. There are areas of undesirable silicon structure (B) and a gas pore (C), which was caused by air entrapment, in a region that otherwise exhibits a normal structure (D). 0.5% HF. 41×. (G.L. Armstrong)

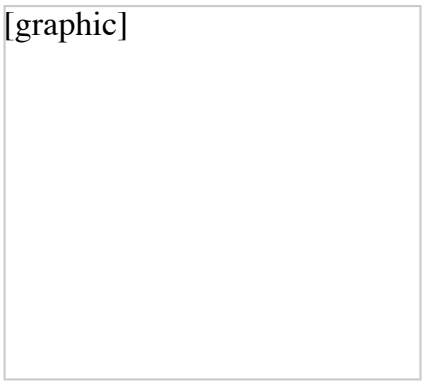
[graphic]

Fig. 176 Gate area (A) of an alloy 413-F die casting that has a cold-shut void (B) and a region of undesirable structure (C and D) surrounded by areas of normal structure (E and F). See also Fig. 177, 178, and 179. 0.5% HF. 11×. (G.L. Armstrong)

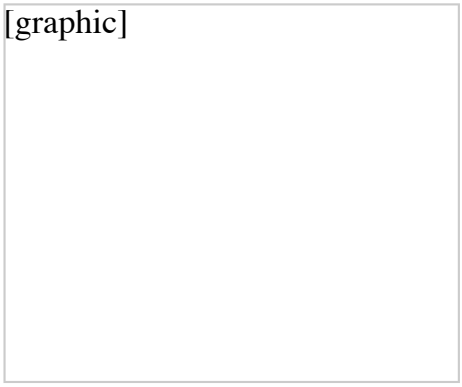
[graphic]

Fig. 177 Area of cold-shut void (A) in Fig. 176. The void resulted when two streams of molten metal failed to merge and interdiffuse. One of the streams produced a normal structure (B), and the other produced an undesirable structure (C). See also Fig. 178 and 179. 0.5% HF. 35×. (G.L. Armstrong)

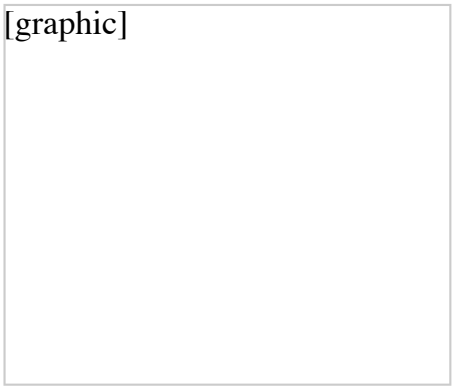
[graphic]

Fig. 178 Inner end of cold-shut void (A) in Fig. 177 showing start of flow line between region of normal structure (B), with eutectic silicon (C) of normal shape in matrix of aluminum solid solution (D), and region of undesirable structure (E). See also Fig. 179. 0.5% HF. 520×. (G.L. Armstrong)

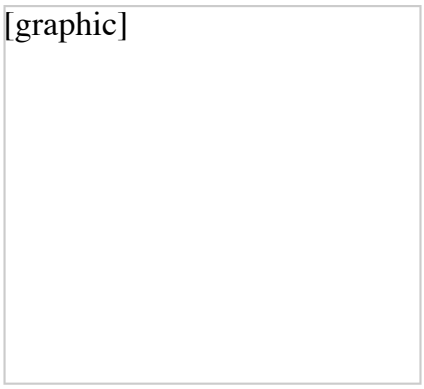

Fig. 179 Continuation of flow line (A) in Fig. 178, separating normal structure (B), with angular silicon (C) in aluminum matrix (D), from undesirable structure (E), with rounded silicon (F) in aluminum matrix (G). Line extends across entire section thickness. 0.5% HF. 520×. (G.L. Armstrong)

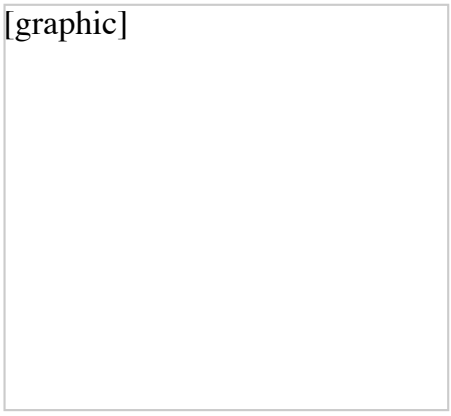

Fig. 180 Alloy 5052-O sheet, 10 mm (0.40 in.) thick, used for weld shown in Fig. 181, 182, and 183. Structure shows particles of $CrAl_7$ (coarse, black). Rounded, outlined areas are pits, where etchant removed Mg_2Si. Keller's reagent. 500×

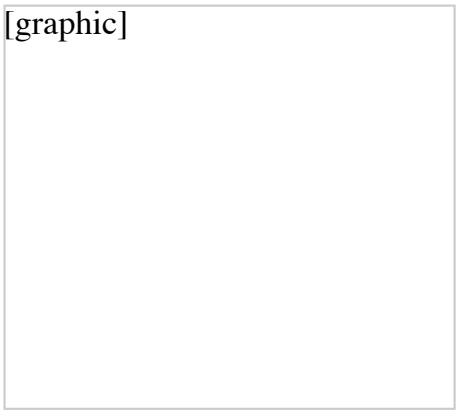

Fig. 181 Heat-affected zone of the weld shown in Fig. 183. Weld bead (see also Fig. 182) was to the right. Structure: equiaxed dendrites of aluminum with much Mg_2Al_3 precipitate near dendrite boundaries forming the dark band in Fig. 183. Keller's reagent. 500×

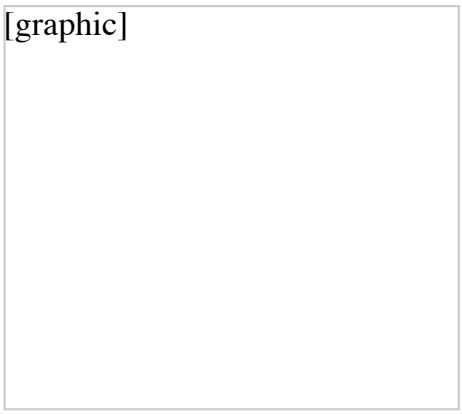
[graphic]

Fig. 182 Bead of the weld shown in Fig. 183. Filler metal was alloy ER5356. The structure consists of equiaxed dendrites of aluminum with a fine precipitate of Mg_2Al_3 (dark) in the dendrites and at dendrite boundaries. Keller's reagent. 500×

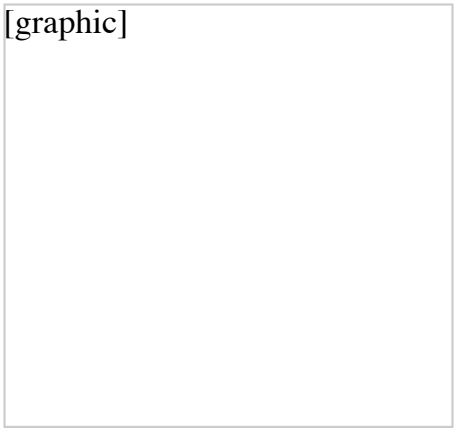
[graphic]

Fig. 183 Gas tungsten-arc fillet weld in alloy 5052-O sheet. Filler metal was alloy ER5356. See also Fig. 180, 181, and 182. Tucker's reagent. 15×

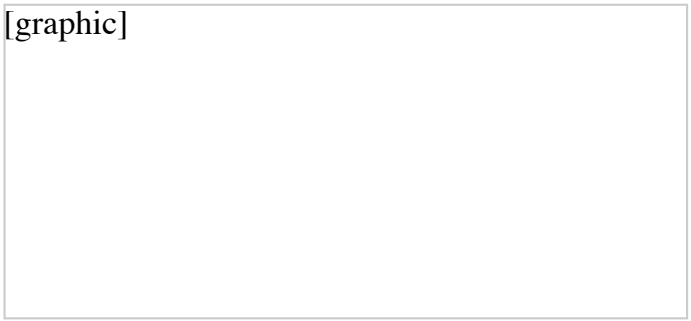
[graphic]

Fig. 184 Gas tungsten-arc weld in a butt joint in alloy 6061-T6 plate, 6.4 mm (0.250 in.) thick. Alternating current and ER4043 filler metal were used. See also Fig. 186 and 188 for other views of the weld. Keller's reagent. 5.5×

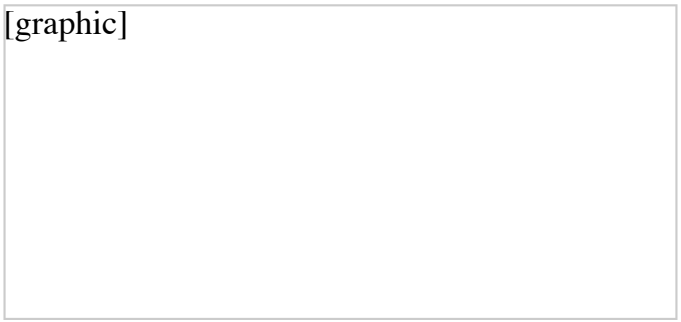
[graphic]

Fig. 185 Gas tungsten-arc weld in a butt joint in alloy 6061-T6 sheet, 1.6 mm (0.063 in.) thick.

Alternating current and ER4043 filler metal were used. Note the extent of the heat-affected zone. See also Fig. 187 and 189. Keller's reagent. 5.5×

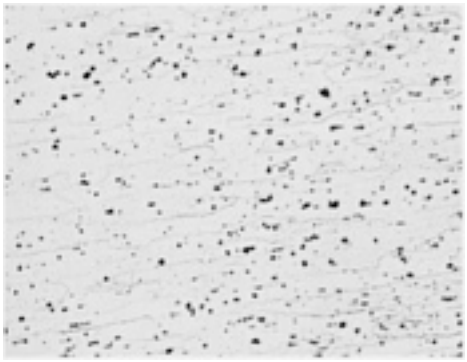

Fig. 186 Structure of 6.4-mm (0.250-in.) thick 6061-T6 plate used in making the weld shown in Fig. 184. Elongated grains of aluminum solid solution contain particles of Mg_2Si (black). See also Fig. 187. Keller's reagent. 100×

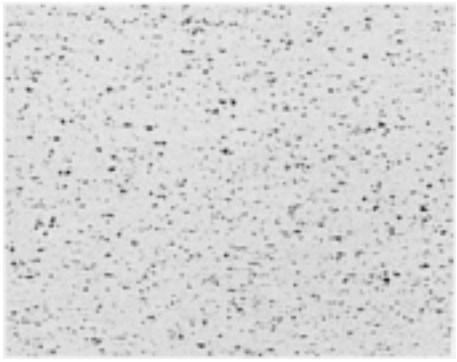

Fig. 187 Structure of 1.6-mm (0.063-in.) thick 6061-T6 sheet used in making the weld shown in Fig. 185. The microstructure is the same as Fig. 186, but contains more Mg_2Si. See Fig. 189 for structure of edge of fusion zone. Keller's reagent. 100×

[graphic]

Fig. 188 Edge of fusion zone of a weld made in 6.4-mm (0.250-in.) thick 6061-T6, using alternating current. Interdendritic network of aluminum-silicon eutectic (dark) in weld bead (right); dark band of Al-Mg_2Si eutectic in the heat-affected zone. Keller's reagent. 100×

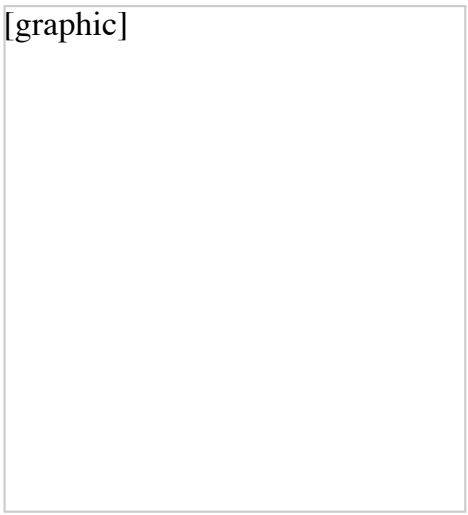

Fig. 189 Edge of fusion zone of a weld made in 6-mm (0.063-in.) thick 6061-T6, using alternating current. The base metal is located on the left and the weld bead is located on the right. The structure is the same as that in Fig. 188, but some porosity (large, black areas) is evident. Keller's reagent. 100×

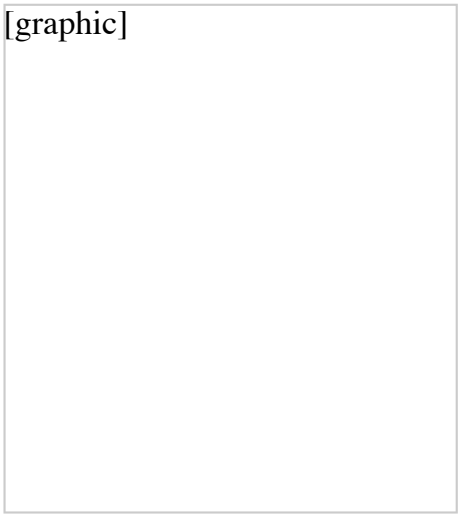

Fig. 190 Edge of fusion zone of a weld made in 6.4-mm (0.250-in.) thick 6061-T6, using straight-polarity direct current. Dark band of Al-Mg_2Si eutectic in heat-affected zone, next to weld bead (right), is narrower and more pronounced than in Fig. 188 (weld made with alternating current). Keller's reagent. 100×

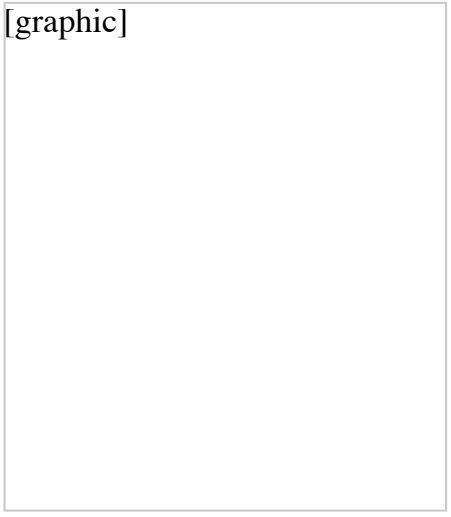

Fig. 191 Edge of fusion zone of a weld made in 1.6-mm (0.063-in.) thick 6061-T6, using straight-

polarity direct current. The microstructure is the same as for the 6.4-mm (0.250-in.) thick plate in Fig. 190, but the amount of interdendritic aluminum-silicon eutectic in the weld bead is greater. Keller's reagent. 100×

[graphic]

Fig. 192 Structure of the 6061-T6 extruded tube (extrusion direction vertical) used for the weld shown in Fig. 193. Black dots are Mg_2Si particles. Keller's reagent. 50×

[graphic]

Fig. 193 Gas tungsten-arc fillet weld joining a 6061-T6 tube (upper left) and an A356-T6 investment casting; ER4043 filler metal. Keller's reagent. 15×

[graphic]

Fig. 194 Structure of A356-T6 investment casting (sodium-modified; grain-refined) used for the weld shown in Fig. 193. Interdendritic network is eutectic silicon. Keller's reagent. 50×

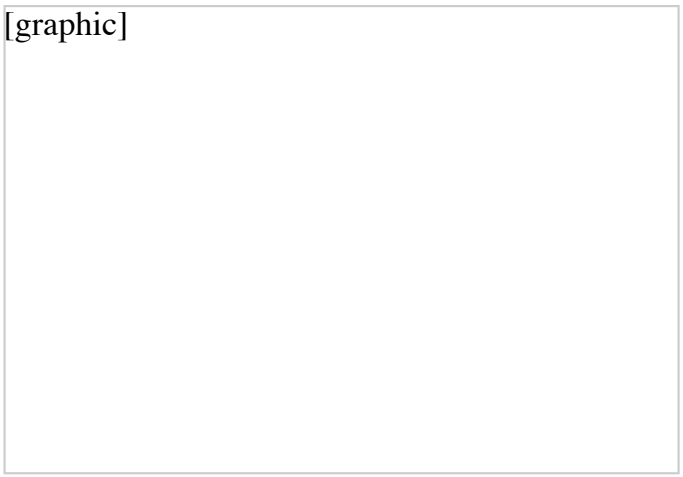
[graphic]

Fig. 195 Edge of the fusion zone of the weld shown in Fig. 193, with the tube at the left and the weld bead at the right. Aluminum-silicon eutectic is present between the dendrites of the weld bead; Al-Mg_2Si eutectic is between the grains of the heat-affected zone of the tube. Keller's reagent. 50×

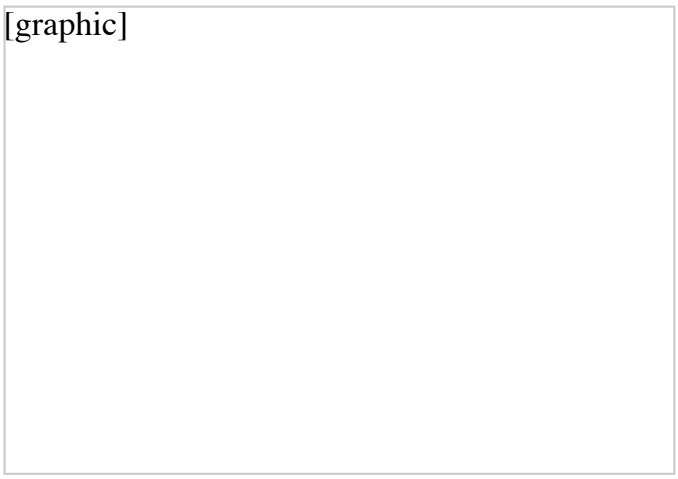
[graphic]

Fig. 196 Edge of the fusion zone of the weld shown in Fig. 193, with the weld bead at top and left and the casting at bottom and right. Interdendritic aluminum-silicon eutectic is present; some in the weld bead, and a large amount in the heat-affected zone of the casting. Keller's reagent. 50×

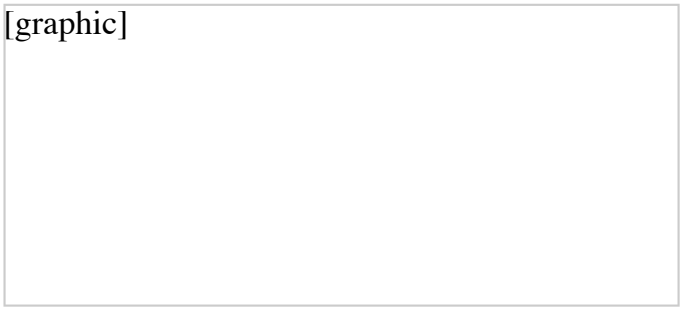
[graphic]

Fig. 197 Bead (near tube) of the weld in Fig. 193. Interdendritic network of aluminum-silicon eutectic is present in the matrix solid solution. Keller's reagent. 50×

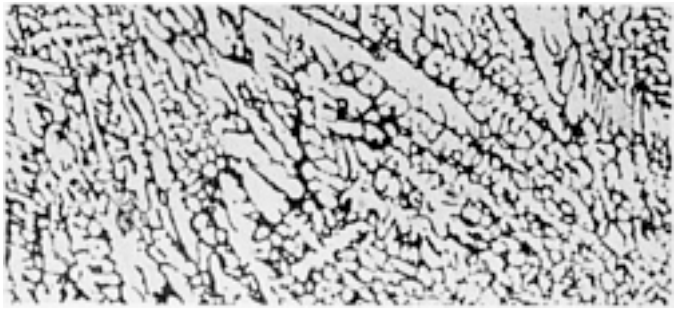

Fig. 198 Bead (near casting) of the weld in Fig. 193. Dendrites of solid solution are less equiaxed, more columnar than in Fig. 197. Keller's reagent. 50×

[graphic]

Fig. 199 Edge of fusion zone of a gas tungsten-arc repair weld in a 356-F investment casting. Alternating current and R-SG70A filler metal were used. Interdendritic aluminum-silicon eutectic (gray); porosity (black). See also Fig. 200. Keller's reagent. 50×

[graphic]

Fig. 200 Same material as Fig. 199, but after solution heat treatment. Particles of eutectic silicon have become rounded and agglomerated. Zone between weld bead and heat-affected zone is less clearly defined than in Fig. 199; porosity remains. Keller's reagent. 50×

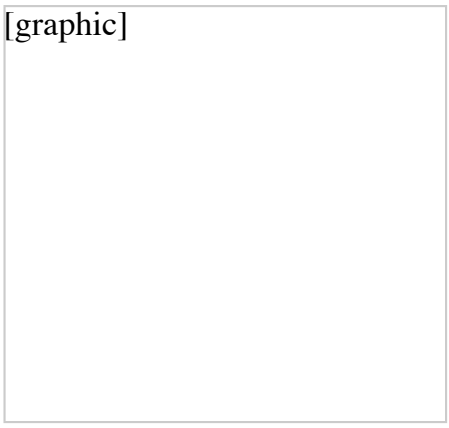

Fig. 201 Structure of 2219-T37 sheet, 3.2 mm (0.125 in.) thick, used for the weld shown in Fig. 202 and 203. Longitudinal section. Elongated grains of solid solution with particles of $CuAl_2$ (light) and $(Fe,Mn)_3SiAl_{12}$ (dark). Keller's reagent. 100×

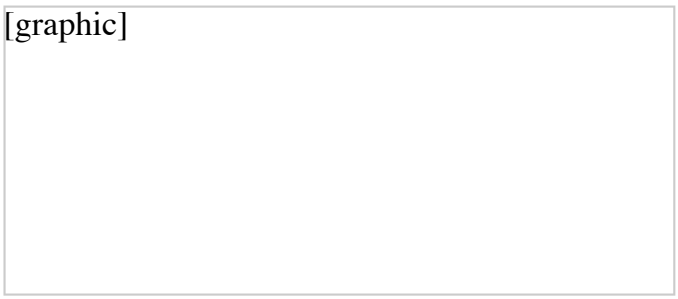

Fig. 202 Gas tungsten-arc weld in a butt joint in alloy 2219-T37 sheet; alloy ER2319 filler metal. See also Fig. 204. Keller's reagent. 10×

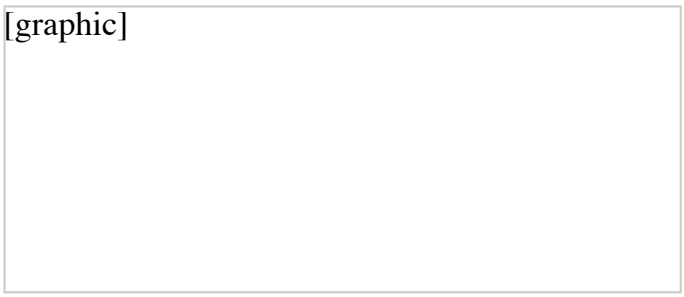

Fig. 203 Electron beam weld in a butt joint in alloy 2219-T37 sheet; alloy ER2319 filler metal. See also Fig. 205. Keller's reagent. 10×

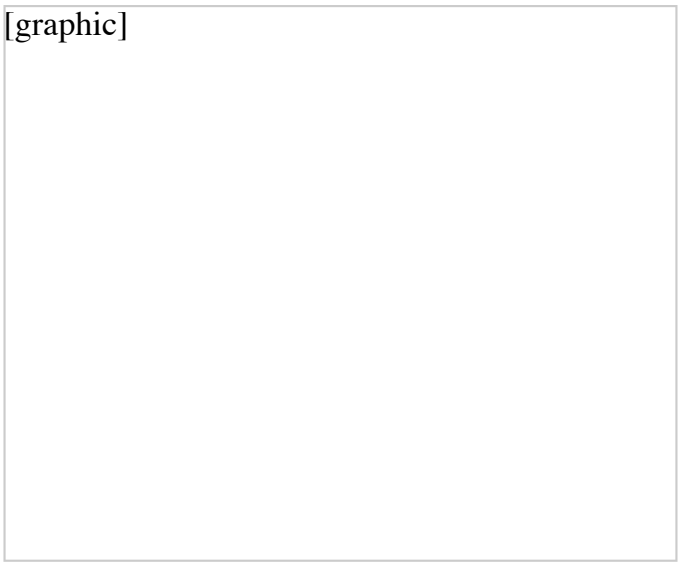

Fig. 204 Edge of the fusion zone of the gas tungsten-arc weld shown in Fig. 202. The base metal is on the left. See also Fig. 205. Keller's reagent. 100×

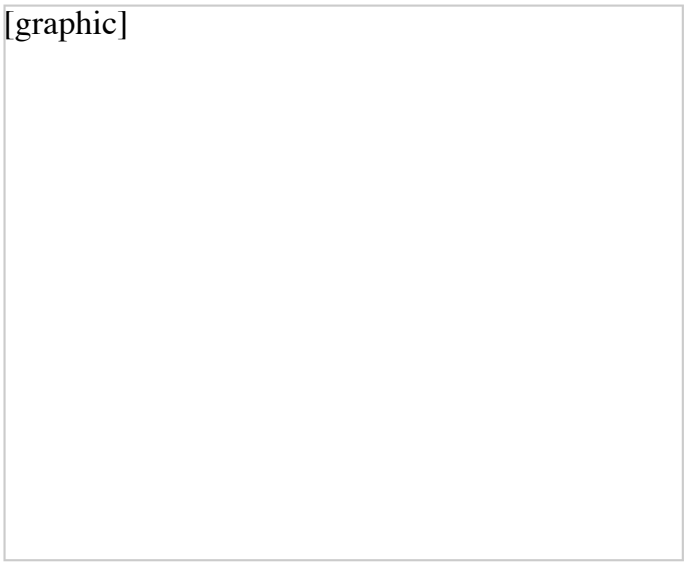

Fig. 205 Edge of the fusion zone of the electron beam weld shown in Fig. 203. The base metal is on the left. Keller's reagent. 100×

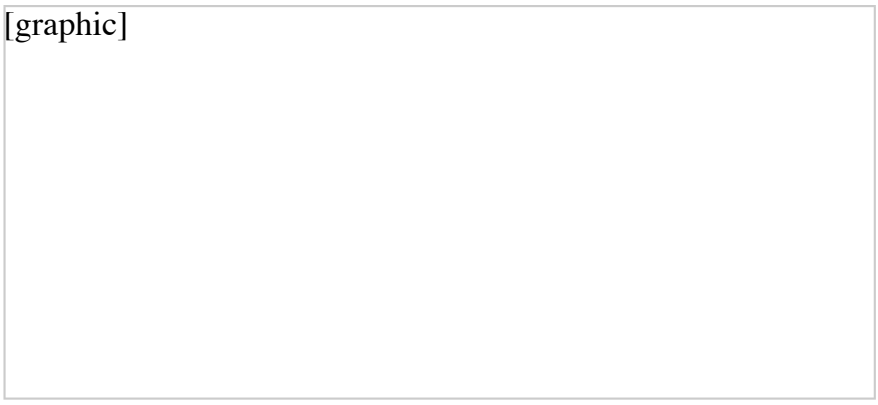

Fig. 206 Electron beam weld in a butt joint in alloy 5456-H321 plate, 25 mm (1 in.) thick. No filler metal was used. See Fig. 207 for details of the edge of the fusion zone. Keller's reagent. 10×

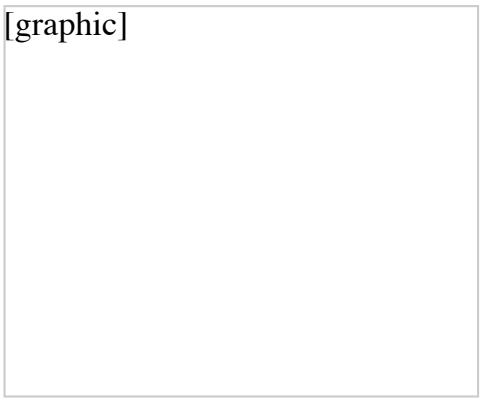

Fig. 207 Edge of fusion zone (base metal is at bottom) of the electron beam weld in Fig. 206. Keller's reagent. 100×

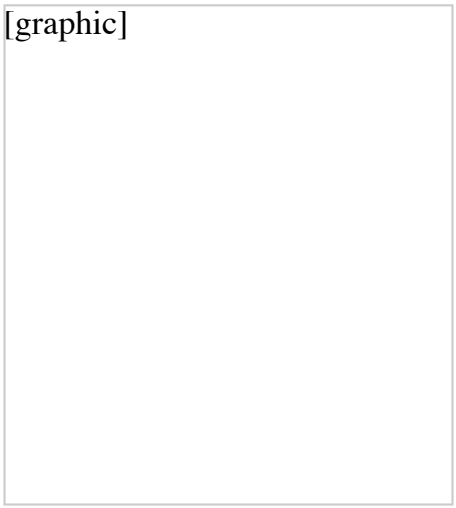

Fig. 208 Electron beam weld in alloy 6061-T6 sheet, 3.2 mm (0.125 in.) thick. No filler metal was used. See Fig. 209 and 210 for details of the edge of the fusion zone. Keller's reagent. 10×

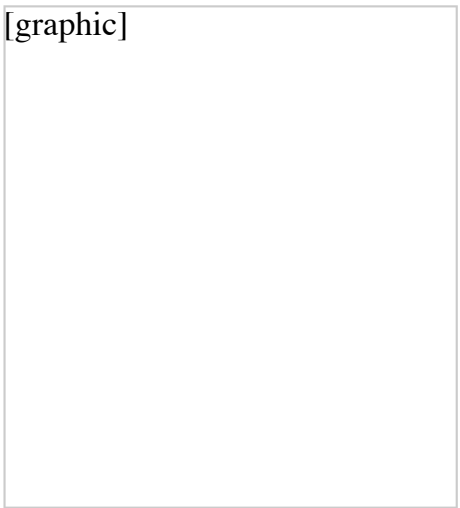

Fig. 209 Edge of the fusion zone (base metal is at left) of the electron beam weld in Fig. 208. Note abrupt change from structure of base metal to that of weld bead. See also Fig. 210. Keller's reagent. 100×

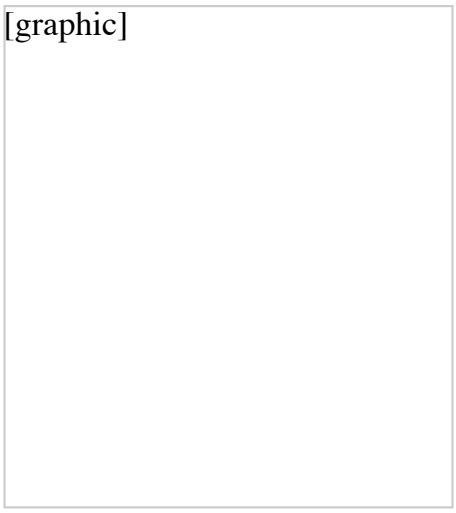

Fig. 210 Same material as Fig. 209, but at a higher magnification. Particles of Mg_2Si (black) and Fe_3SiAl_{12} (gray) in base metal (left) and interdendritic Al-Mg_2Si eutectic in weld metal. Keller's reagent. 500×

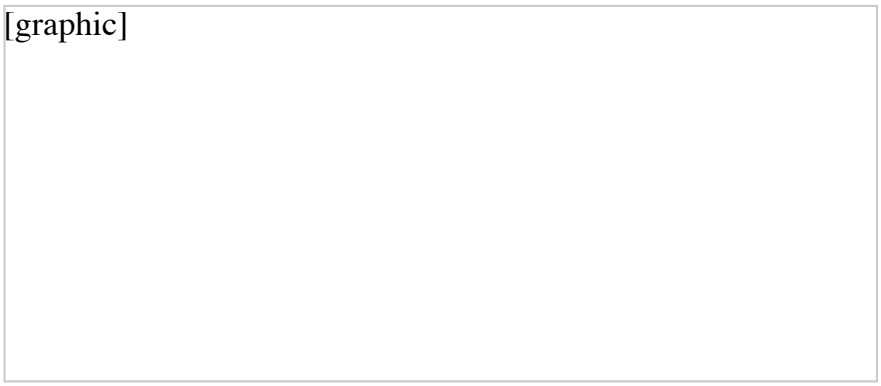

Fig. 211 Electron beam weld in a butt joint in alloy 7039-T63 plate, 25 mm (1 in.) thick. No filler metal was used. See Fig. 212 for details of the edge of the fusion zone. Keller's reagent. 10×

Fig. 212 Edge of fusion zone (base metal is at bottom) of the electron beam weld in Fig. 211. Keller's reagent. 100×

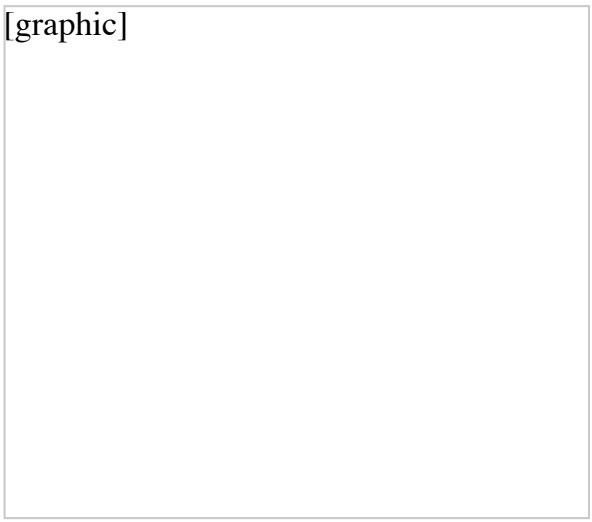

Fig. 213 Electron beam weld in an alloy 295-T6 investment casting. Weld was made without filler metal. Overheating during welding resulted in a considerable amount of dropthrough (right), with accompanying longitudinal shrinkage cracks in the center of the weld metal. See also Fig. 214. Tucker's reagent. 5×

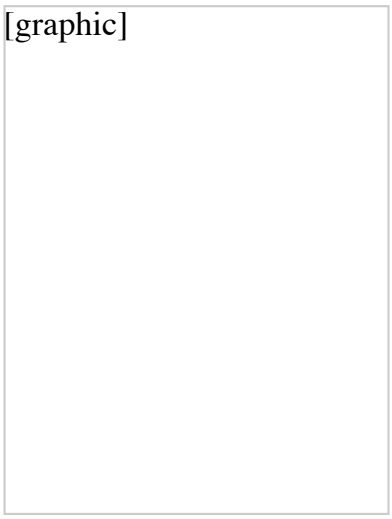

Fig. 214 Edge of fusion zone of weld shown in Fig. 213 (base metal at bottom). Large dendrites of solid solution in base metal, small dendrites in weld bead; Al-$CuAl_2$-Si eutectic in both. Keller's reagent.150×

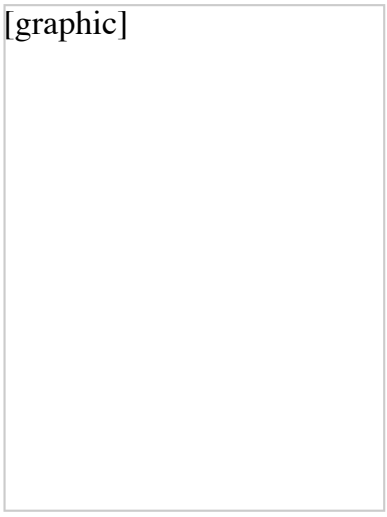

Fig. 215 Core of alclad 2024-T4 sheet used in resistance spot weld shown in Fig. 216. The dark

particles are $CuMgAl_2$, CU_2MnAl_{20}, and CU_2FeAl_7; light particles, $CuAl_2$· See also Fig. 217, 218, 219, and 220. Keller's reagent. 500×

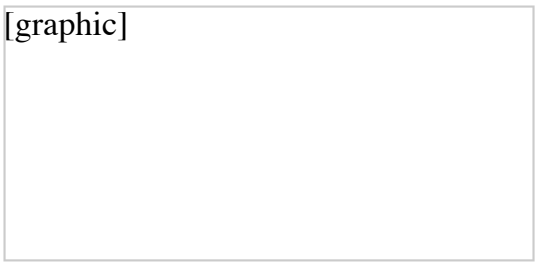

Fig. 216 Resistance spot weld in 2024-T4 sheets clad with alloy 1230. Oval nugget has zone of columnar grains surrounding equiaxed grains. See also Fig. 217, 218, 219, and 220. Tucker's reagent. 10×

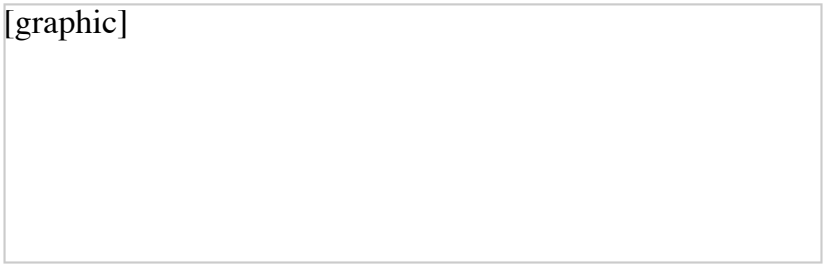

Fig. 217 Inner zone of nugget of the resistance spot weld shown in Fig. 216. The structure consists of small equiaxed grains. This inner zone is surrounded by an outer zone that consists of columnar grains. See also Fig. 218. Keller's reagent. 500×

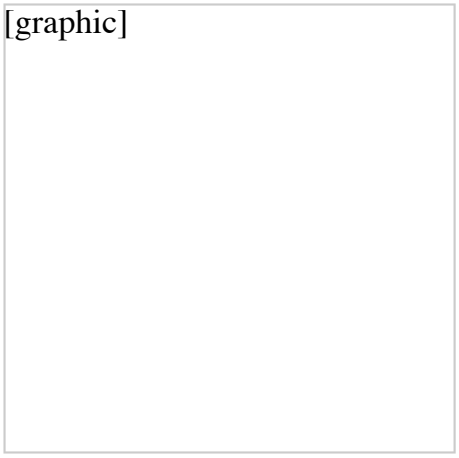

Fig. 218 Outer zone of nugget of the weld shown in Fig. 216. Columnar grains are normal to the edge of the nugget. See also Fig. 217, which shows inner zone of nugget. Keller's reagent. 550 ×

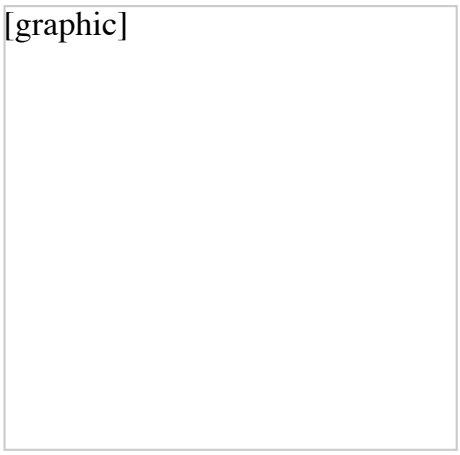
[graphic]

Fig. 219 Transition zone of the weld in Fig. 216 showing eutectic segregation-depletion (light band) at edge of nugget and concentration (dark band) in the base metal. Keller's reagent. 550×

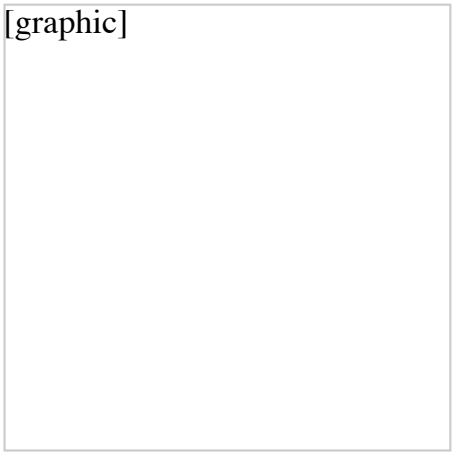
[graphic]

Fig. 220 Outer zone of nugget (at interface) of resistance spot weld made in alclad 2024-T4 sheets. Unfused cladding (right) projects into the weld nugget. See also Fig. 216. Keller's reagent. 550 ×

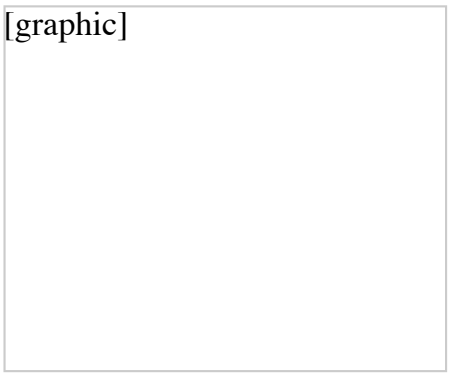
[graphic]

Fig. 221 Explosive welded joint between aluminum sheet (top) and steel showing characteristic ripples at the interface. A ripple is shown at a higher magnification in Fig. 222. As-polished. 6×

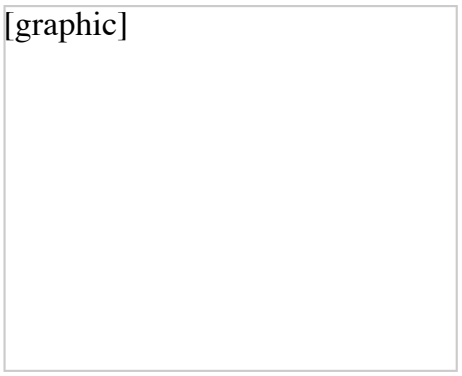

Fig. 222 Ripple at interface of explosive welded joint between aluminum sheet (top) and steel. Cracks have appeared in the dark-gray phase (which probably is $FeAl_3$). As-polished. 60×

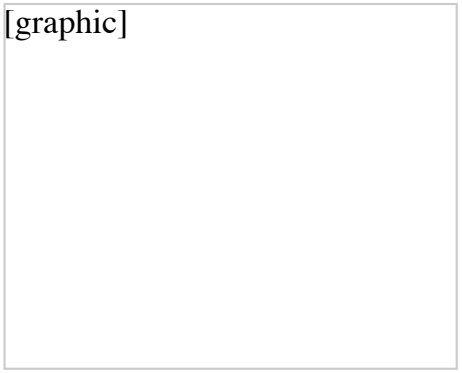

Fig. 223 Explosive welded joint between aluminum sheet (top) and copper. Cracks (black) have appeared in the aluminum-copper phase (light gray) at the relatively smooth interface. As-polished. 225×

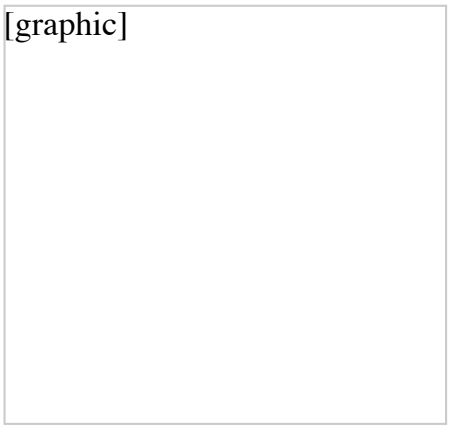

Fig. 224 Pressure weld (cold) in alloy 2014-T6 bar. The flow lines at the joint show the movement of metal toward the edge of the bar during weld upsetting. 0.5% HF. 150×

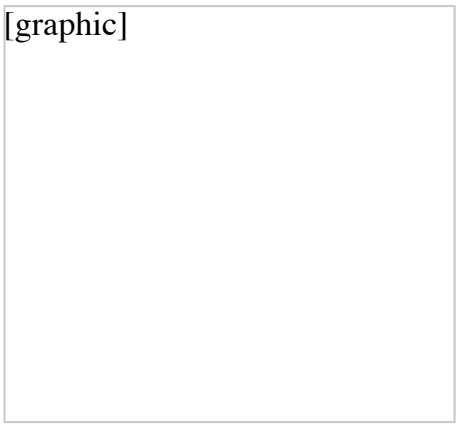
[graphic]

Fig. 225 Brazed joint between 6063-O sheets, made with 4047 (BAlSi-4) filler metal. See Fig. 226 for details of structure of the smaller fillet. As-polished. 5×

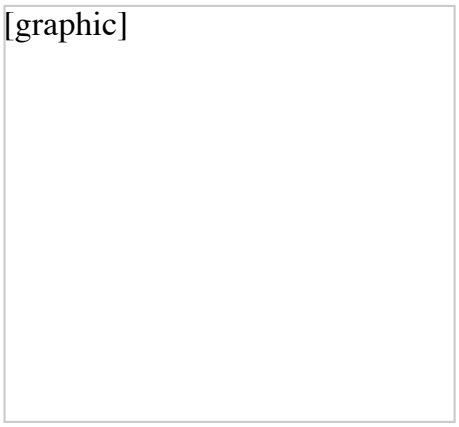
[graphic]

Fig. 226 Smaller fillet of brazed joint shown in Fig. 225. Structure consists of dendrites of aluminum solid solution (light gray) and aluminum-silicon eutectic matrix (dark). As-polished. 50×

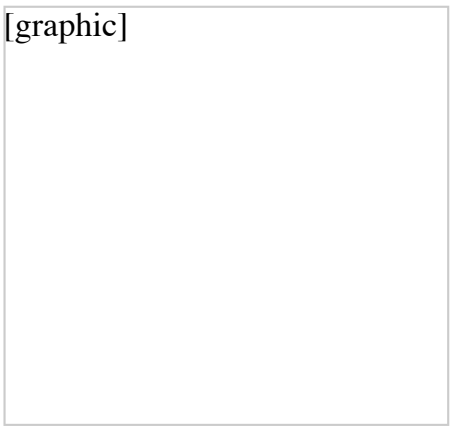
[graphic]

Fig. 227 Brazed joint between alloy 7004-O sheets, made with alloy 4245 filler metal. See Fig. 228 for details of the microstructure of the larger fillet. As-polished. 5×

[graphic]

Fig. 228 Larger fillet of brazed joint shown in Fig. 227. Structure consists of dendrites of aluminum solid solution (light), matrix of aluminum-silicon eutectic (mottled), and particles of primary silicon (dark). As-polished. 50×

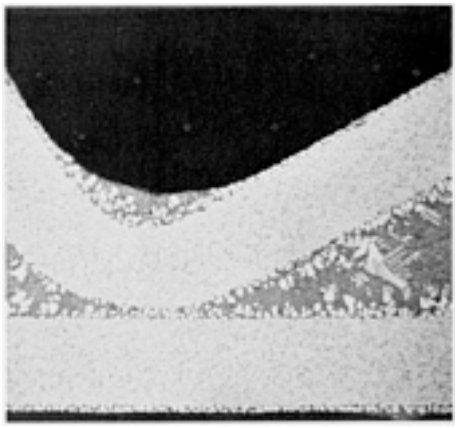

Fig. 229 Brazed joint in 12-O brazing sheets (alloy 3003 clad on both sides with alloy 4343 filler metal). Fillets show dendrites of solid solution (light) in aluminum-silicon eutectic matrix. 0.5% HF 30×

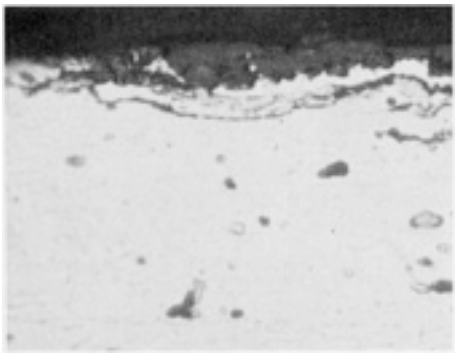

Fig. 230 Surface fretting (dark gray) on 3.2-mm (0.125-in.) thick alloy 7075-T651 sheet that was fayed to a 4130 steel strap in a fatigue test. Fretting corrosion product is Al_2O_3. Keller's reagent. 1050×

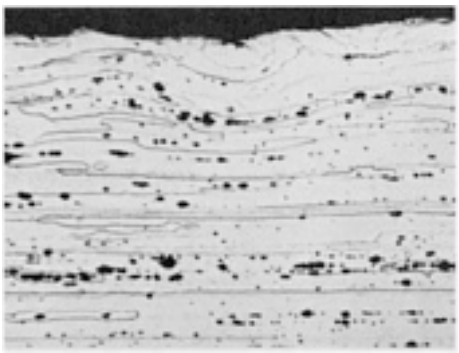

Fig. 231

[graphic]

Fig. 232

Alloy 7075-T651 sheet showing the effect of saturation peening. Fig. 231: longitudinal section. Fig. 232: transverse section. The sheet was peened with S230 cast steel shot to an Almen-gage intensity of 0.006 to 0.008 A. The surface of the sheet (at the top) shows deformation and roughening. Keller's reagent. 150×

[graphic]

Fig. 233 Surface at top of electrochemically machined hole in 25-mm (1-in.) thick 7075-T651 plate, showing roughness. Keller's reagent. 50×

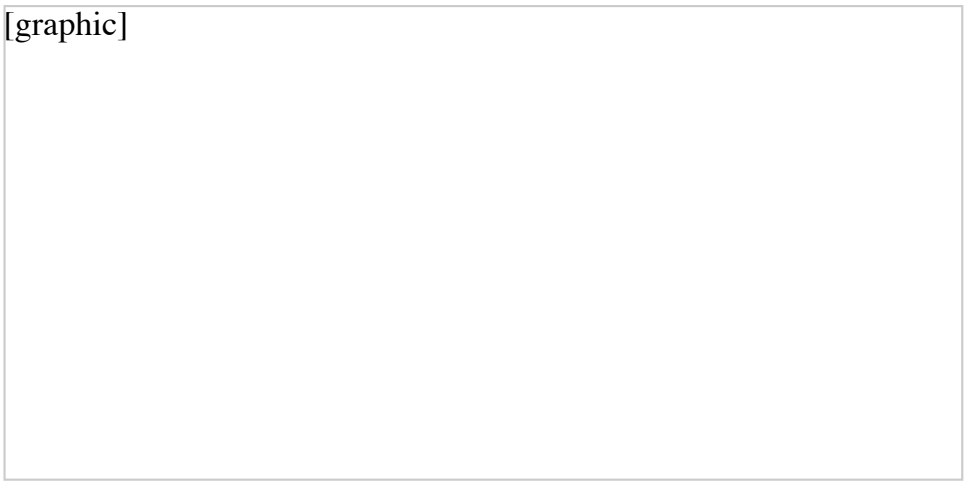

Fig. 234 Section through machined threads in an alloy 2024-T4 extruded bar, 25 mm (1 in.) diam, showing a typical degree of surface roughness on thread flanks. Machining burrs have been left on the crests of the threads. Microstructure is essentially unworked. See also Fig. 236. Keller's reagent. 100×

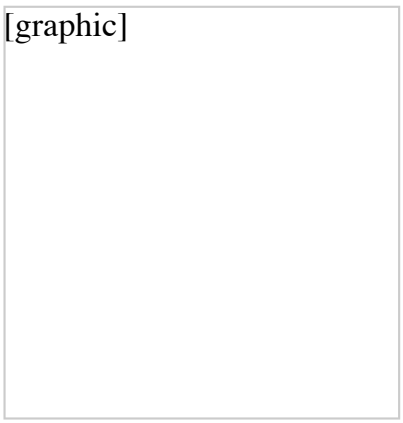

Fig. 235 Surface midway through electrochemically machined hole in 25-mm (1-in.) thick 7075-T651. Relatively smooth. Keller's reagent. 50×

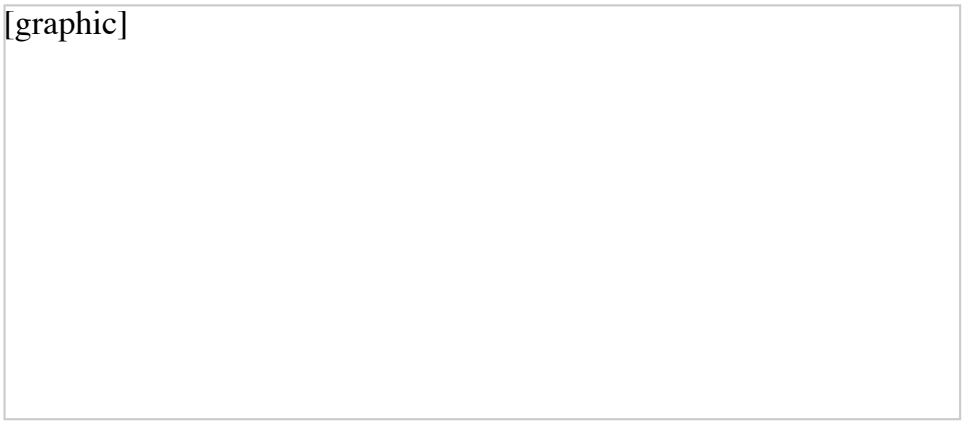

Fig. 236 Section through cold-rolled threads in an alloy 2024-T4 extruded bar, 25 mm (1 in.) diam, showing highly worked structure in metal at thread flanks. Deformed metal almost completely encloses a cavity at crest of each thread; this is an undesirable condition. Compare machined threads in Fig. 234. Keller's reagent. 100×

<Previous section in this article